Identifying interfacial mechanisms limitations within aqueous Zn-MnO2 batteries and means to cure them with additives

Ivette Aguilar, Pierre Lemaire, Nawfel Ayouni, Ezzoubair Bendadesse, Anatolii V Morozov, Ozlem Sel, Véronique Balland, Benoît Limoges, Artem M Abakumov, Encarnacion Raymundo-Piñero, et al.

To cite this version:

Ivette Aguilar, Pierre Lemaire, Nawfel Ayouni, Ezzoubair Bendadesse, Anatolii V Morozov, et al.. Identifying interfacial mechanisms limitations within aqueous Zn-MnO2 batteries and means to cure them with additives. Energy Storage Materials, 2022, 53, pp.238-253. 10.1016/j.ensm.2022.08.043 . hal-03791355

HAL Id: hal-03791355
https://hal.science/hal-03791355v1

Identifying interfacial mechanisms limitations within aqueous Zn-MnO_2 batteries and means to cure them with additives

Ivette Aguilar[a,b,c], Pierre Lemaire[a,b,c], Nawfel Ayouni[a], Ezzoubair Bendadesse[a,b,c], Anatolii. V. Morozov[d], Ozlem Sel[a,c], Véronique Balland[e,*], Benoît Limoges[e], Artem M. Abakumov[d], Encarnacion Raymundo-Piñero[f,c], Aneta Slodczyk[g], Aurélien Canizares[f], Dominique Larcher[h,c] and Jean-Marie Tarascon[a,c,*]

a) Chimie du solide et de l'Energie, UMR 8260, Collège de France, Paris Cedex 05 75231, France
b) Sorbonne Université, Paris 75005, France
c) Réseau sur le Stockage Electrochimique de l'Energie (RS2E), CNRS FR 3459, Amiens Cedex 80039, France
d) Center for Energy Science and Technology, Skolkovo Institute of Science and Technology, Nobel str. 3, 121205 Moscow, Russia
e) Université Paris Cité, CNRS, Laboratoire d'Electrochimie Moléculaire, F-75013 Paris, France
f) Conditions Extrêmes Et Matériaux : Haute Température Et Irradiation CEMHTI, CNRS UPR 3079, Université d'Orléans, Orléans Cedex 2, France
g) Laboratoire de dynamique, interactions et réactivité (LADIR) UMR 7075, CNRS and Sorbonne Université, Paris 75005, France
h) Laboratoire de Réactivité et chimie des solides (LRCS), UMR CNRS 7314, Université de Picardie Jules Verne, Amiens Cedex, France

Corresponding authors: veronique.balland@u-paris.fr, jean-marie.tarascon@college-de-france.fr

Abstract

Li-ion batteries are playing a key role within the field of electrical mobility, grid applications and related objects owing to their high energy densities and long lifetime, but their sustainability remains to be improved. Pushing in this direction, there is a rising interest towards rechargeable aqueous batteries. Great efforts are devoted to turn the primary alkaline zinc-manganese dioxide batteries that have dominated the primary battery applications into rechargeable systems. This turns out to be a colossal task owing to the complexity of the Zn-MnO_2 chemistry that is not yet fully rationalized, thus causing delay in practical deployment. In this work we revisit this chemistry by combining fundamental solution chemistry considerations and complementary analytical techniques (TEM, Raman spectroscopy and EQCM) together with the assembly of cells using either MnO_2 or MnO_2-free initial positive electrodes. We confirm the key role of the electrolyte together with the inseparable link between its pH and the system's electrochemical response. Moreover, during discharge and charge, we provide experimental evidence for the occurrence of MnO_2 electrodissolution and back electrodeposition conjointly with the formation of soluble zinc hydroxides up to chemical precipitation and back dissolution of a $Zn_4SO_4(OH)_6.xH_2O$ phase. We show that this phase is essential in the buffering of the system's pH and demonstrate the beneficial role of its initial presence in the positive electrode composite. Further pushing the idea of buffering the pH of the electrolyte, we propose the use of additives such as ZnO, $Mg(OH)_2$ or $La(OH)_3$ that enhance the capacity retention upon cycling, while slightly penalize the cell capacity. These insights provide missing links regarding the interplay between the conjoint electrochemical-chemical reactions ruling the functioning of rechargeable Zn-MnO_2 batteries, hence providing a step forward towards their development.

1. Introduction

Great hope is placed in the use of renewable energies to limit the depletion of fossil-fuel resources. However, to make good use of wind or sun intermittent energies, we need grid-scale energy storage systems for peak shaving and load shifting. To this end, the Li-ion battery technology offers the greatest number of merits if its sustainability and safety are increased and its cost keeps decreasing below 100$ per kWh stored, as foreseen for 2025.[1] These concerns are presently driving research towards alternative systems, namely Na-ion, Li-S, Li-air, with extensive recent efforts devoted to aqueous systems such as Li(Na)-ion, Zn-air, Zn-MnO_2.[2]–[4]

However, none of these water-based technologies can presently rival the 100 $/kWh of Li-ion, as the threefold voltage penalty is associated to the thermodynamic stability range of water, limited to 1.23 V. Great hopes have recently been placed in the use of super-concentrated electrolytes (Water In Salt Electrolyte, WISE) which broaden the operational water potential range to 2-3 V.[5] However, although quite elegant, the practical aspect of such an approach for Li-aqueous system is uncertain because of poor capacity retention as well self-discharge at 55°C due mainly to the reduction of H_2O at the negative electrode.[6] Another option towards more sustainable batteries and departing from Li(Na) based aqueous systems is provided by the resurge of interest in reversible aqueous Zn-MnO_2 batteries (denoted as Zn insertion batteries, ZIB) based on the controversial belief that Zn^{2+} acts as a guest ion alike Li^+ in MnO_2-type insertion host.[7], [8] The large abundance of both Mn and Zn together with the high volumetric capacity of Zn anodes (5851 mAh/cm^3) render this sustainable aqueous system highly appealing for large-scale applications.

Zinc has always been a fascinating element for electrochemists since it was the inherent anode part of the Volta's pile in 1800 and of the Daniel's pile in 1836. It was equally adopted later on by Leclanché (1868) in its first Zn-MnO_2 pile based on a saline electrolyte, which enjoyed through the years of various chemical and engineering modifications to become the alkaline Zn-MnO_2 primary batteries (~1950) used for decades to power toys, flash-lights, home electronic devices and medical units to name only a few applications. They deliver energy densities ranging from 80 to 190 Wh.kg^{-1}.[9] It is not for lack trying that such batteries could not be made rechargeable but because of huge difficulties encountered in mastering issues such as formation of Zn dendrites and corrosion, precipitation of by-products, irreversible phase transition…[10]–[12] These trials were not vain since rechargeable aqueous cells relying on the use of KOH-based gel electrolyte plus specific additives were commercialized by Rayovac under the brand name of Renewal (1992).[13] However, their cycle life was strongly dependent upon their depth of discharge and limited to around 25 cycles for depth of discharge greater than 50 %, hence the sale speech of a primary battery with extra capacity.

Moreover, surveying a variety of electrolytes Yamamoto et al. report back in 1986,[14] the benefits of $ZnSO_4$-based aqueous electrolyte for improving the reversibility, but this finding was not followed till 2012 where Xu et al.[15] demonstrated the feasibility to reach a sustained reversibility up to 100 cycles by using a slightly acidic ($ZnSO_4$, $Zn(NO_3)_2$) electrolyte. This finding has received worldwide attention and led to a blossoming of research activities centered on mastering the reversibility of the Zn-MnO_2 aqueous system. Great advances were made with the identification of an optimized mild acid electrolyte (2 M $ZnSO_4$ + 0.2 M $MnSO_4$) that enables to reach more than 5000 cycles for Zn-MnO_2 coin cells cycled at high rates (> 5 C) for weakly loaded electrodes (< 1 mg/cm^2).[16]–[19] Such a finding was followed with numerous studies aiming towards a full understanding of the chemical-electrochemical reaction mechanism underlying the performance of the Zn-MnO_2 system at the component and cell level. This has yielded a prolific literature with numerous proposed scenarios: (*i*) reversible Zn^{2+} insertion into the host MnO_2 structure to produce either layered Zn-birnessite, Zn-buserite, or spinel $ZnMn_2O_4$,[8], [15], [20]–[27] (*ii*) reversible insertion of protons to form hausmannite (Mn_3O_4)[28] or manganese oxyhydroxide (MnOOH) according to a solid-solution[29], [30] or a conversion type reaction[16], [31] (*iii*) co-insertion of H^+ and Zn^{2+} into MnO_2 according to different thermodynamic paths and chemical reactions, [19], [32]–[36] and (*iv*) reversible proton-coupled electrodissolution-electrodeposition of MnO_2.[37]–[45] Moreover, in all mechanisms involving protons (*ii* to *iv*), precipitation of Zn- or Zn-Mn layered double hydroxides has been observed during cell discharge, and attributed to a local pH increase due to proton consumption.

Such a variety of mechanisms is all the more intriguing as most of the systems studied present common electrochemical features, with the charge-discharge voltage traces exhibiting, beyond the first cycle, a smooth two-plateau staircase on charge and a sloping discharge disrupted by a voltage hint. It is worth noting that there is currently no consensus nor clear explanation for the voltage hint observed in the discharge curve and how it relates to the two plateaus during the charge. The field is thus still waiting further insights for mastering the Zn-MnO_2 system's complexity.

In the present work, we revisited the Zn-MnO_2 electrochemistry starting with the inspiring work of Yamamoto *et al.*[14], [28] prior to check some of the previous findings and proposed a reaction mechanism to reconcile most of the experimental facts. Based on a comprehensive analysis of pH–variation through cycling, we propose an approach to buffer the system by cathode additives, hence enabling a sustained reversibility even at low rates.

2. Experimental

2.1. Materials

$ZnSO_4.7H_2O$ (99%,), $MnSO_4.4H_2O$ (99%, Alfa Aesar), acetic acid (99%+), $MnCl_2$. H_2O, Carbon black Super P conductive (62M^2/g), Zn disk (98% 0.75 mm thick), KOH (99.98%), 1-Methyl-2-pyrrolidinone (Biograde 99.5 %) were purchased from Alfa Aesar. Sodium acetate (99%), $Na_2S_2O_8$,(98%), H_2O_2 30% (w/w) (analytical grade), HNO_3 65% Suprapur, 10% PTFE (prepared from Polytetrafluoroethylene, 60 wt % dispersion in water) was acquired from Sigma aldrich. Deionized water was generated by MilliQ system and had a resistivity of 18 Ω. Membrane filters (mixed cellulose ester, 0.2µm porosity) and Glass microfiber separator were purchased from Whatman tm. PVDF-HFP (Kinar), EMD-ɣ-MnO_2 (Tekkosha), β-MnO_2 (Prolabo). All reagents were used as received without any further treatment.

CMD-γ-MnO_2 was synthetized by adding 50ml of 0.6 M of $Na_2S_2O_8$ into a round bottom flask containing 125ml of 0.2M $MnSO_4$ under heating and magnetic stirring. The resulting precipitate was washed several times with MilliQ water, filtered through a cellulose ester filter and dried at 100°C under vacuum (büchi vacuum pump) for 20 hours. ZHS was synthetized by mixing 2M KOH and 2M $ZnSO_4$ solutions in stoichiometric amounts and stirred for 20 minutes in air. The white powder was then filtered and washed several times with water. The remaining product was dried at 70°C in air.

2.2. Methods

TEM analysis (*Electron diffraction (ED) patterns, (HAADF-STEM) images, energy-dispersive X-ray (EDX) spectra, STEM-EDX compositional maps, and electron energy loss (EELS) spectra*) were acquired on a probe aberration-corrected FEI Titan Themis Z electron microscope at 200 kV, equipped with a Super-X system for energy-dispersive X-ray (EDX) analysis and Gatan Quantum ER965 spectrometer. The energy resolution, measured from the full width at half maximum of the zero-loss peak, was 0.9 eV. **pH titrations** were done using a HQ430D (HACH)Single Input Lab Multimeter coupled to a classical analogue pH meter. **The Quantification of dissolved O_2** were done using Hach LDO101 Standard with a digital, luminescent/optical probe coupled to HQ430D (HACH) Single Input Lab Multimeter. **X-Ray Diffraction** (XRD) was carried out on a D8 ADVANCE diffractometer (Bruker) using a Cu Kα X-ray source (1.5406Å). Peaks were attributed using the PDF-2 /release 2013 RDB database.**The Galvanostatic cycling was** performed using a VMP3 or VMP-300 potentiostat from BioLogic (the cycling protocols are detailed in Supplementary information). **In situ Raman analyses** were carried out using a Renishaw RA100 spectrometer coupled to a (CCD) camera. The spectra were collected using a 50x objective, a 514nm laser (at 10% power), and an exposure time of 300s. **The quantification of Mn^{2+}** either from the material or from the electrolyte was achieved on a Nexion 2000B inductively coupled plasma atomic Mass spectrometer (Perkin-Elmer) using the Syngistix™ software. **Scanning Electron Microscopy** (SEM) images were acquired on a SU-70 Hitachi FEGSEM (accelerating voltage: 5 kV**). EQCM measurements** were performed on a commercial SEIKO QCM922A microbalance using AT-cut 9 MHz quartz resonators patterned with gold.

3. Results and discussion

3.1. Inspiration from early work – a journey with the Yamamoto cell

Initial evidence of sustained reversibility was first reported by Yamamoto *et al.*[14] in laboratory cells using a Zn disc as negative electrode, a composite positive electrode prepared of 40 mg of electrochemically-made (EMD) γ-MnO_2 and 10 mg of Super P carbon (C_{sp}), both being separated by a glass fiber separator hosting 200 µL of an aqueous solution of $ZnSO_4$ (2 M, pH = 3.7). A cell made under similar conditions confirms the published results (**SI-0, supplementary information**), with a reversible capacity of ca. 3 mAh. Interestingly, alike in Yamamoto's papers, beyond the first cycle, the charge-discharge voltage traces exhibit a smooth two-plateau staircase on charge and a sloping discharge disrupted by a voltage hint. **(Figure 1A-**right panel**)**. This feature is commonly observed in the hundreds of published papers on that topic, independently of the exact composition of the electrolyte or the type of MnO_2 used [46], that suggests a unique charge storage mechanism. Noteworthy, the precipitation of Zn-based layered double hydroxides during the cell discharge associated to a proton-consuming discharge process was already evidenced in Yamamoto's early work, assuming Mn_3O_4 as the main reduction product.[28]

To get more insights into the reaction process, and notably on the first discharge which is rarely discussed in the literature, despite of its unique profile, we carried out an ICP quantitative analysis of the Mn content in the cathode during cycling for various Zn/MnO_2 cells containing initially either EMD-γ-MnO_2 (electrochemically-made), CMD-γ-MnO_2 (chemically-made) or β-MnO_2 **(Figure 1B, Figure S1)**. The cells were cycled between 0.85 and 1.75V at a current of +/- 1 mA and stopped once either the first discharge or the first full discharge/charge cycle was completed, prior recovering and quantifying the remaining MnO_2 from the cathode mixture. From the collected elemental contents we deduced that 2.6 mg, 2.9 mg and 10.6 mg of MnO_2 are dissolved during the first discharge of the EMD, β-MnO_2 and CMD cells, respectively, which correspond to dissolution of 19%, 26% and 65% of the initial amount of MnO_2 (**SI-1, Figure S2, supplementary information**). With respect to the discharge capacity, such mass loss indicates that between 1.85 and 2 e^- are exchanged per dissolved Mn atom. These results reveal an electrochemical mechanism driven by the 2-electron/4-proton reductive dissolution of MnO_2 into Mn^{2+} (eq. 1), independently of the starting MnO_2 phase. The highest capacity (*i.e.*, highest mass dissolved) is obtained for CMD-γ-MnO_2, which is made of smaller particles as deduced by SEM (**Figure 1B**). However, the obtained capacities remained low owing to our inability to fully use our starting MnO_2 materials. Interestingly, the addition of a redox mediator into the electrolyte, alike what has been recently done with Li-air systems, was shown to unlock the capacity from the non-electroactive MnO_2.[47]

$$(1)\quad MnO_{2\,(s)} + 2e^- + 4\,H^+ \rightarrow Mn^{2+}{}_{(aq)} + 2\,H_2O$$

The origin of the proton in this mechanism of electro-dissolution of MnO_2 is a key question, unfortunately often overlooked. Contrary to a general belief, water is not the proton source since MnO_2 shows a purely capacitive behaviour in aqueous electrolytes containing only an inert salt.[38] It is worth noting that the 2 M $ZnSO_4$ electrolyte consists mainly of Zn^{2+} ions solvated by six water molecules. The solvated zinc aqua complex $[Zn(H_2O)_6]^{2+}$ is a well-known weak Brønsted di-acid characterized by two close pK_a values (*i.e.*, 8.96 and 8.86 for the first and second deprotonation reaction, respectively).[48] Accordingly, it can behave as a proton donor at the MnO_2/electrolyte interface,[38] leading after a first deprotonation step to the intermediate amphoteric $[Zn(H_2O)_5(OH)]^+$ complex (eq. 2), which itself can further deprotonate to lead to the neutral double hydroxide $Zn(H_2O)_4(OH)_2$ species (eq. 3). Owing to the very low solubility of $Zn(H_2O)_4(OH)_2$, it precipitates as Zn-layered double hydroxides, which in the presence of co-precipitated SO_4^{2-} can slowly convert into the crystalline form of $Zn_4SO_4(OH)_6.5H_2O$ (or ZHS).[16], [29], [35], [39], [41], [49]

$$(2)\quad MnO_{2\,(s)} + 2\,e^- + 4\,[Zn(H_2O)_6]^{2+} \rightarrow Mn^{2+}{}_{(aq)} + 4\,[Zn(H_2O)_5(OH)]^+ + 2\,H_2O$$
$$(3)\quad MnO_{2\,(s)} + 2\,e^- + 4\,[Zn(H_2O)_5(OH)]^+ \rightarrow Mn^{2+}{}_{(aq)} + 4\,[Zn(H_2O)_4(OH)_2] + 2\,H_2O$$

It is therefore difficult to specify the exact protonation state of the zinc complexes involved in the reductive electro-dissolution of MnO_2 and, for sake of simplicity, the best is to propose the overall reaction ascribed in eq. 4:

$$(4)\quad MnO_{2\,(s)} + 2\,e^- + 2\,[Zn(H_2O)_6]^{2+} \rightarrow Mn^{2+}{}_{(aq)} + 2\,Zn(OH)_{2\,(s)} + 10\,H_2O$$

where $Zn(OH)_{2\,(s)}$ is the precursor for the local formation of ZHS. It is important to note that, similarly to $Zn^{2+}{}_{(aq)}$, the $Mn^{2+}{}_{(aq)}$ ions have a weak Bronsted di-acidity (pK_a)[50] and they also can participate as proton donors to assist the electrodissolution of MnO_2, as evidenced on model electrodes,[38] and then precipitate as a double hydroxide, to finally lead into the formation of a Zn-Mn-layered double hydroxide or $Mn_xZn_y(OH)_zSO_4{\cdot}5H_2O$, (ZnMnLDH) as recently reported by Wilkinson *et al*.[42]

Although reductive electrodissolution applies to all three MnO_2 phases, important differences on the first discharge voltage profile have been observed (**Figure 1B left-column**). Indeed, β-MnO_2 is marked by a well-defined discharging plateau at 1.2 V, that is not present in the case of CMD- or EMD-γ-MnO_2 for which the cell voltage shows progressive decrease from a much higher potential value. We hypothesize these differences to be nested in a varying initial pH of the electrolyte arising from the surface states of the pristine materials. To test this hypothesis, we placed 50 mg of each MnO_2 into 50 mL of distilled water and note that the pH of the supernatant raised by two units for β-MnO_2, and by 0.5 for EMD-γ-MnO_2 and CMD-γ-MnO_2. This is in line with the mismatch observed in the β-MnO_2 cells, and the lower value of the discharge potential which we attribute to a higher initial pH. Indeed, according to the Nernst law of eq. 1, the discharge potential for the electrodissolution of MnO_2 is expected to vary by 120 mV per pH unit,[38] most likely allowing early precipitation of ZHS (**Figure 1B**, **bottom left**).

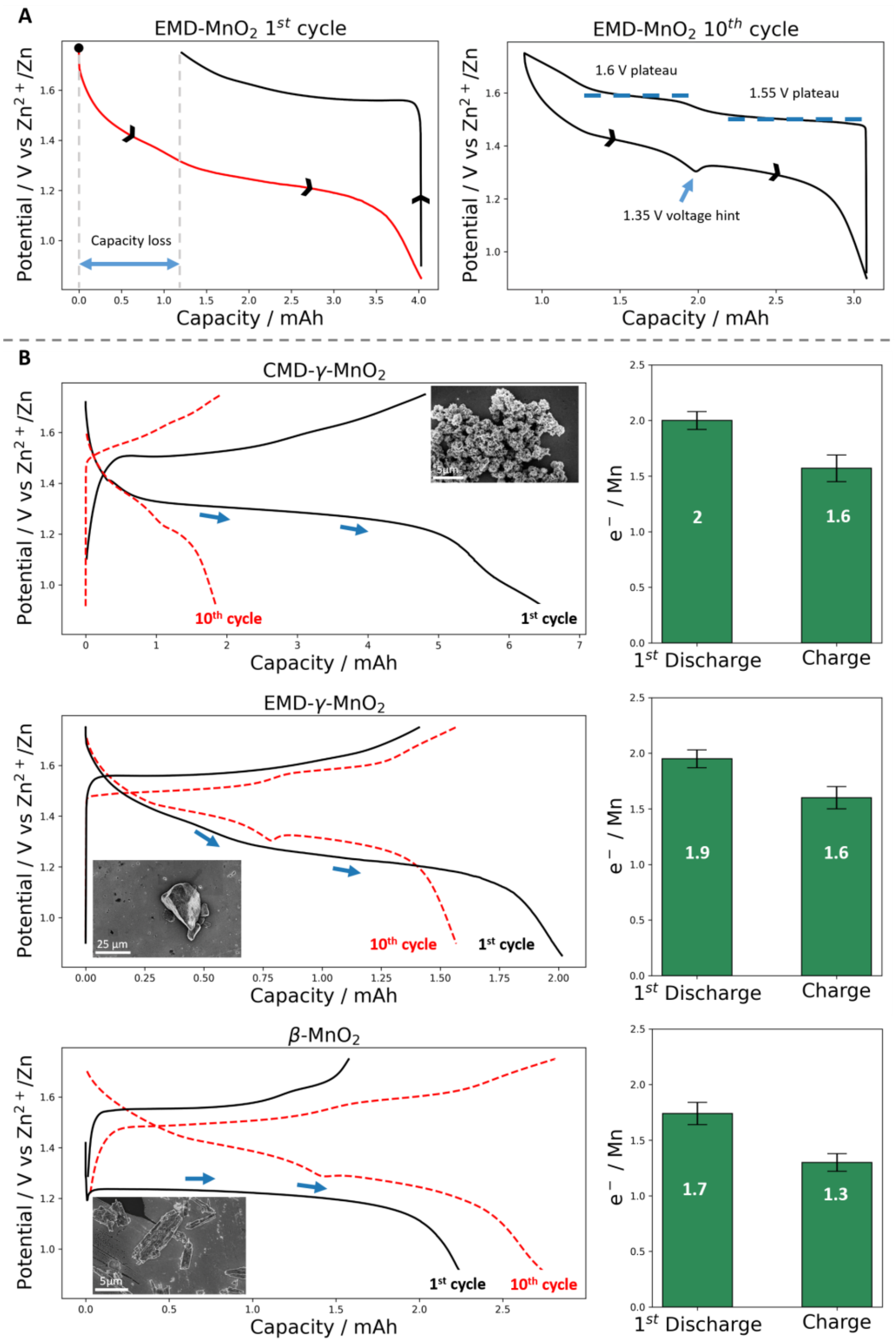

Figure 1. (A) Galvanostatic profiles at +/- 2 mA of the (left) 1st and (right) 10th cycle of an EMD-γ-MnO_2/Zn cell. Cell started on discharge. Yamamoto's conditions.[14], [51] Cathode: 40 mg of EMD-γ-MnO_2 mixed with 10 mg of Super P carbon powder. Electrolyte: 200 µL of 2 M $ZnSO_4$. Anode: Zn foil. Temperature: 25°C. **(B)** Comparison between the 1st (black plain lines) and 10th (dashed red lines) galvanostatic cycling profiles at +/- 1 mA of CMD-γ-MnO_2/Zn (top row), EMD-γ-MnO_2/Zn (middle row) and β-MnO_2/Zn (bottom row) cells. Cells started on discharge. Yamamoto's conditions.[14], [51] Cathode: 20 mg of MnO_2 mixed with 5 mg of Super P carbon powder. Electrolyte: 100 µL 2 M $ZnSO_4$. Anode: Zn foil. Temperature: 25°C. SEM images of the pristine cathode materials are given as insets in the left column. Right column: number of electrons exchanged per dissolved/deposited Mn determined using ICP quantification and Faraday's law.

In the following charging step, ICP results show that the cathode regains its initial mass in Mn whatever the cell considered, which indicates back electrodeposition of manganese oxide by re-oxidation of Mn^{2+} produced on discharge. Moreover, the slight capacity decrease upon the following charge, independently of the pristine MnO_2 type (**Figure 1B**, **right column**), suggesting that the redox state of the newly electrodeposited Mn-oxide is significantly lower than that of pristine MnO_2. The number of electrons exchanged per Mn atom deduced from ICP is indeed equal to ~1.6 in all cells, which indicates that the same oxidation product is formed independently of the MnO_2 we started with. Afterwards, all cells could be reversibly cycled (see 10th cycle plotted in **Figure 1B**), with the galvanostatic curves exhibiting two plateaus at charge and a voltage hint at 1.3 V at discharge.

Overall, the above results show the sustained reversibility of the Zn-MnO_2 system in a Mn^{2+}-free electrolyte, while recent studies stated that a Mn^{2+} additive is mandatory for good cyclability.[20], [52] We thus added 0.2 M $MnSO_4$ to the electrolyte of the cells assembled as above but no modifications were observed in the degree of dissolution (**Figure S3, Supplementary information**).This confirms that the Mn^{2+} additive does not impede the reductive dissolution of MnO_2 but simply prevents Mn^{2+} depletion at the electrode/electrolyte interface during the back electrodeposition process.[38] Besides, it also allows for over-deposition of MnO_2 during the charge, leading finally to an artificial increase of the cathode gravimetric capacity.

To interrogate the way the partial dissolution-precipitation occurs, we conducted SAED, HAADF-STEM, EDX, and EELS measurements on *ex-situ* samples recovered from cells based on C_{sp}-EMD-γ-MnO_2 composites (see **Supplementary information SI-2** for the experimental details) that were (*1*) discharged, (*2*) discharged-charged once, and (*3*) discharged-charged ten times between 0.85 and 1.75V (Yamamoto's conditions, **Figure 2**). STEM-EDX maps of the sample 1 (after first discharge, **Figure 2A, left panel**) reveal two phases, identified as ZHS and γ-MnO_2. The ZHS phase lacks crystallinity and can only be recognized in STEM-EDX compositional maps as particles enriched with jointly Zn and S (**Figure 2A left-panel**), while SAED patterns of γ-MnO_2 can be confidently indexed to a *C*2/*m* monoclinic structure with $a \approx 13.7$ Å, $b \approx 2.9$ Å, $c \approx 4.5$ Å, $\beta \approx 90.5^\circ$ (**Figure 2A right -panel**). HAADF-STEM images demonstrate a typical rutile-ramsdellite intergrowth structure (mixing of the 1x1 and 1x2 tunnels formed by edge-sharing MnO_6 octahedra) consisting of nanosized [130]/[010] twinned domains. Such structure is ascribed to our remaining pristine γ-MnO_2 (compare to **Figure S4, Supplementary information**), thus confirming a discharge mechanism based on electrodissolution of MnO_2 and local precipitation of ZHS. The sample morphology drastically changes at the end of the following charge (sample 2) with namely a significant decrease in the size of ZHS agglomerates (**Figure 2B**). Besides, we identified the presence of two Mn-based phases with different Zn:Mn ratios. The first phase has a Zn:Mn atomic ratio of 8:92 with a monoclinic γ-MnO_2 structure as the one identified in sample 1 (**Figure 2B,** right panel 1), which corresponds to the pristine material. The second phase contains both Zn and Mn and forms intertwined fibres with poor crystallinity. The SAED pattern indicates that this phase adopts the structure of hexagonal ε-MnO_2 akhtenskite (sp. gr. *P*6$_3$/*mmc*). However, the presence of the broad prominent diffraction ring at ~3.55 Å suggests an additional Mn-Zn ordering since this ring cannot be indexed with the referenced akhtenskite structure.[53] STEM-EDX elemental maps show Zn: Mn atomic ratio of 25:75 in the ε-(Zn,Mn)O_2 akhtenskite. In addition, the Mn valence state in this phase was calculated as +3.3 by EELS, which implies with great certainty that Zn is an intrinsic part of the charged phase. Hence, we attributed this second phase to $Zn_{0.33}MnO_2$ (**Figure 2B left**). This finding is not specific to cells based on EMD-γ-MnO_2 since HAADF-STEM images and SAED patterns of CMD-γ-MnO_2 and *β*-MnO_2 also reveal some $Zn_{0.33}MnO_2$ phase upon the first charge (**Figures S5 – S9, Supplementary information**). Furthermore,

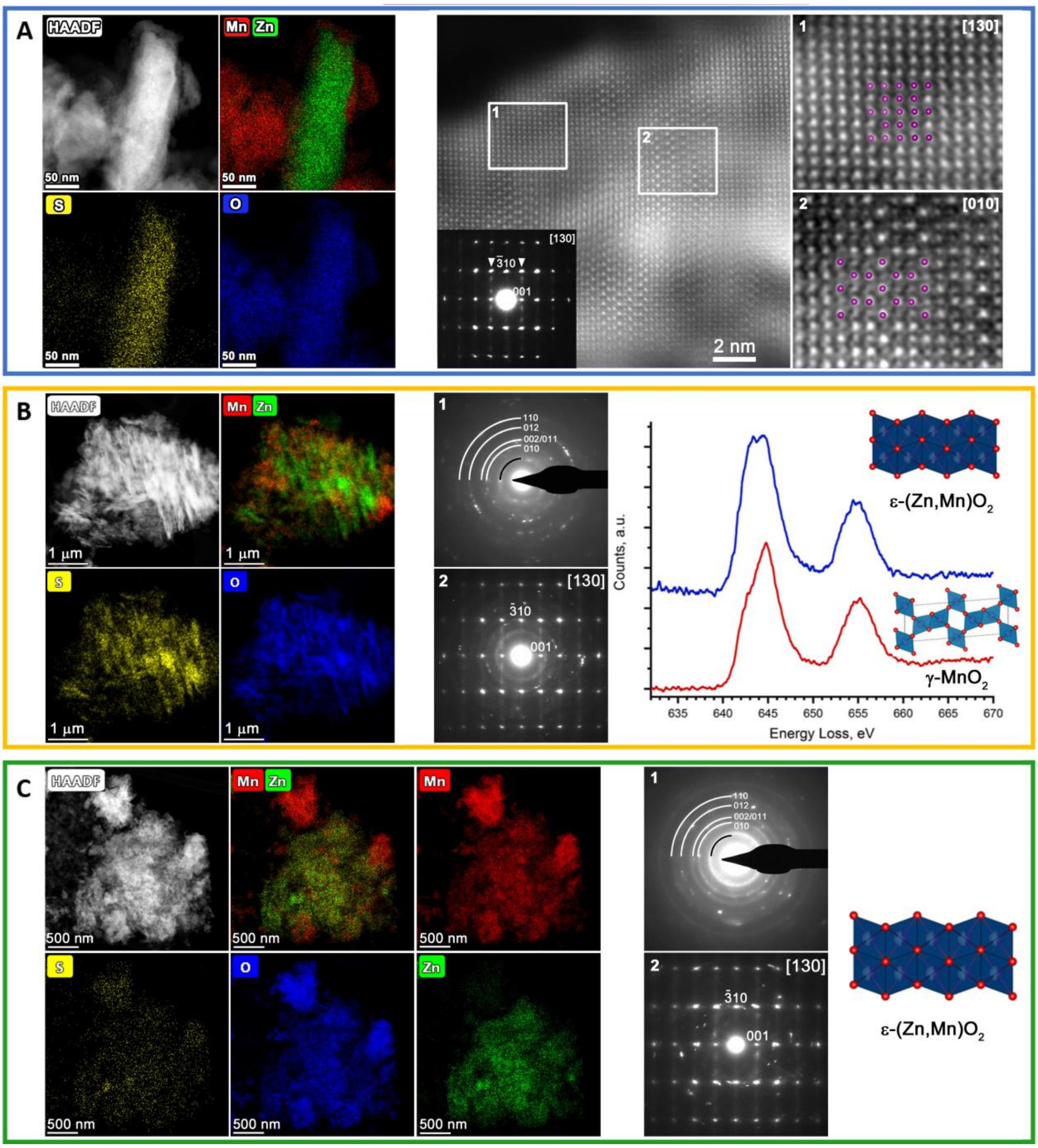

Figure 2. (A) (left) HAADF-STEM image and EDX maps for Zn, Mn, S and O in the sample 1 (after 1st discharge) containing γ-MnO_2 and $Zn_4SO_4(OH)_6{\cdot}xH_2O$. **(A) (right)** HAADF-STEM image and corresponding SAED pattern of γ-MnO_2. White arrowheads in the SAED pattern indicate diffuse reflections from the overlapping [130]- and [010]-oriented domains. White rectangles ("1" and "2") indicate the [130] and [010] domains of the γ-MnO_2 structure (shown enlarged at the right with the Mn atoms overlaid as purple spheres). **(B) (left)** HAADF-STEM image and EDX maps for Zn, Mn and S in the sample 2 (after 1st charge) **(B) (right)** SAED patterns of the two phases observed in the sample 2: ε-$(Zn,Mn)O_2$(1) and γ-MnO_2 (2) along with their representative Mn-$L_{2,3}$ EELS edges. **(C) (left)** HAADF-STEM image and EDX compositional maps for Zn, Mn, O and S in the sample 3 (after 10th charge). **(C) (right)** SAED patterns of the two phases observed in the sample 3: ε-$(Zn,Mn)O_2$ (1) and γ-MnO_2 (2), Mn:Zn similar to the sample 2

this $Zn_{0.33}MnO_2$ phase has also been clearly identified in the sample 3 (10th charge) in high amounts (**Figure 2C)**, signing its accumulation over cycling. The formation of $Zn_{0.33}MnO_2$ during the electrodeposition of MnO_2 implies a lower number of electrons exchanged per Mn atom than for the pristine MnO_2. However, the e^-/Mn^{2+} ratio of 1.6 deduced from ICP (see above) is significantly higher than the value of 1.3 associated to the formation of $Zn_{0.33}MnO_2$, so we assume MnO_2 to be also formed during the charge.

Lastly, it is worth mentioning that no spinel-structured phases were ever detected in the samples 1-3. Thus, the presence of the $Zn_{0.33}MnO_2$ after the first charge and its growth upon subsequent charges (**Figures S10-S13, Supplementary information**) testifies that the growth-nucleation of this phase results from an electrochemical triggering of chemical reactions upon oxidation, rather than any type of Zn^{2+} insertion process.[43], [44], [54] Although our observations indicate a major path involving Mn-oxide growth and dissolution, subtle process variations can be observed depending on the nature of the pristine material. Indeed, $ZnMn_2O_4$ tetragonally distorted spinel phase has been detected in β-MnO_2 and CMD-γ-MnO_2 after 10th cycle in contrast to EMD-γ-MnO_2 for reasons we cannot explain, but their contribution is minimal. Moreover we should recall that such a spinel phase was already reported and its growth explained from a $Mn_xZn_y(OH)_2SO_4.5H_2O$.[42] (**Figures S14- S17, Supplementary information**).

In any case, such early journey through the Zn-MnO_2 system teaches us that from the beginning its cyclability in a mild acidic 2 M $ZnSO_4$ aqueous electrolyte is associated to a reversible electrodissolution/electrodeposition reaction, coupled to a complex precipitation/dissolution process. However, at that time, owing to the lack of quantitative analysis together with the system's complexity, reaching a final conclusion regarding the mechanism was difficult. As always in such a situation, there is a need to simplify the system. So from now on, our cells will be initially MnO_2-free, if not otherwise specified, and thus be started on charge to promote the electrodeposition of Mn-oxides *in situ*.

3.2. From MnO_2 electrodes to electrodeposited MnO_2 electrodes

Since the electrodeposition of MnO_2 requires a Mn^{2+}-containing electrolyte, we selected the 2 M $ZnSO_4$ + 0.2 M $MnSO_4$ composition (pH 3.7) in reference to previous works.[19] Mn-oxide was electrodeposited on carbon black C_{sp} (super P® from Alfa Aesar) (62 m^2/g) in a Swagelok cell containing 700 µL of electrolyte with Zn foils as counter and reference electrodes. The electrodeposition performed at a constant current of 60 µA shows a single plateau at ~1.9 V (*vs*. Zn^{2+}/Zn) in **Figure 3A**. The electrodeposited material was next characterized *ex-situ* by Raman spectroscopy, XRD and SAED. The Raman spectrum exhibits bands in the 500-700 cm^{-1} range specific of MnO_2 compounds[55] (**Figure S18A, Supplementary information**), while XRD, and SAED reveal the presence of a hexagonal ε-MnO_2 phase with an akhtenskite-type structure (**Figures S18B** and **S18C, Supplementary information**) with the particles showing a very small Zn:Mn atomic ratio (6:94) as deduced from EDX analysis. The minute amount of detected Zn corresponds most likely to electrolyte residuals (**Figure S19, Supplementary information**) since the SAED ring at 3.55 Å characteristic of the Zn/Mn ordering in $Zn_{0.33}MnO_2$ is absent in such pattern.

The amount of MnO_2 electrodeposited was quantified by ICP (see **Supplementary information SI-4** for the experimental details). Interestingly, it is inferior to the theoretical weight (close to 50%) deduced from Faraday's law considering the 2-electron oxidation of Mn^{2+} into MnO_2. The departure from 100% is likely rooted in the oxygen evolution reaction (OER)[56] as a consequence of the strong acidification of the electrolyte resulting from the release of 4 H^+ per MnO_2 electrodeposited (eq. 5), spawning thus the voltage plateau at almost 1.9 V. This has been confirmed by an *in situ* monitoring of the dissolved oxygen concentration (measured with a digital luminescent/optical probe (see **Supplementary information SI-5** for the experimental details).

$$(5)\ Mn^{2+}{}_{(aq)} + 2\ H_2O \rightarrow \varepsilon\text{-}MnO_{2\ (s)} + 2\ e^- + 4\ H^+{}_{(aq)}$$

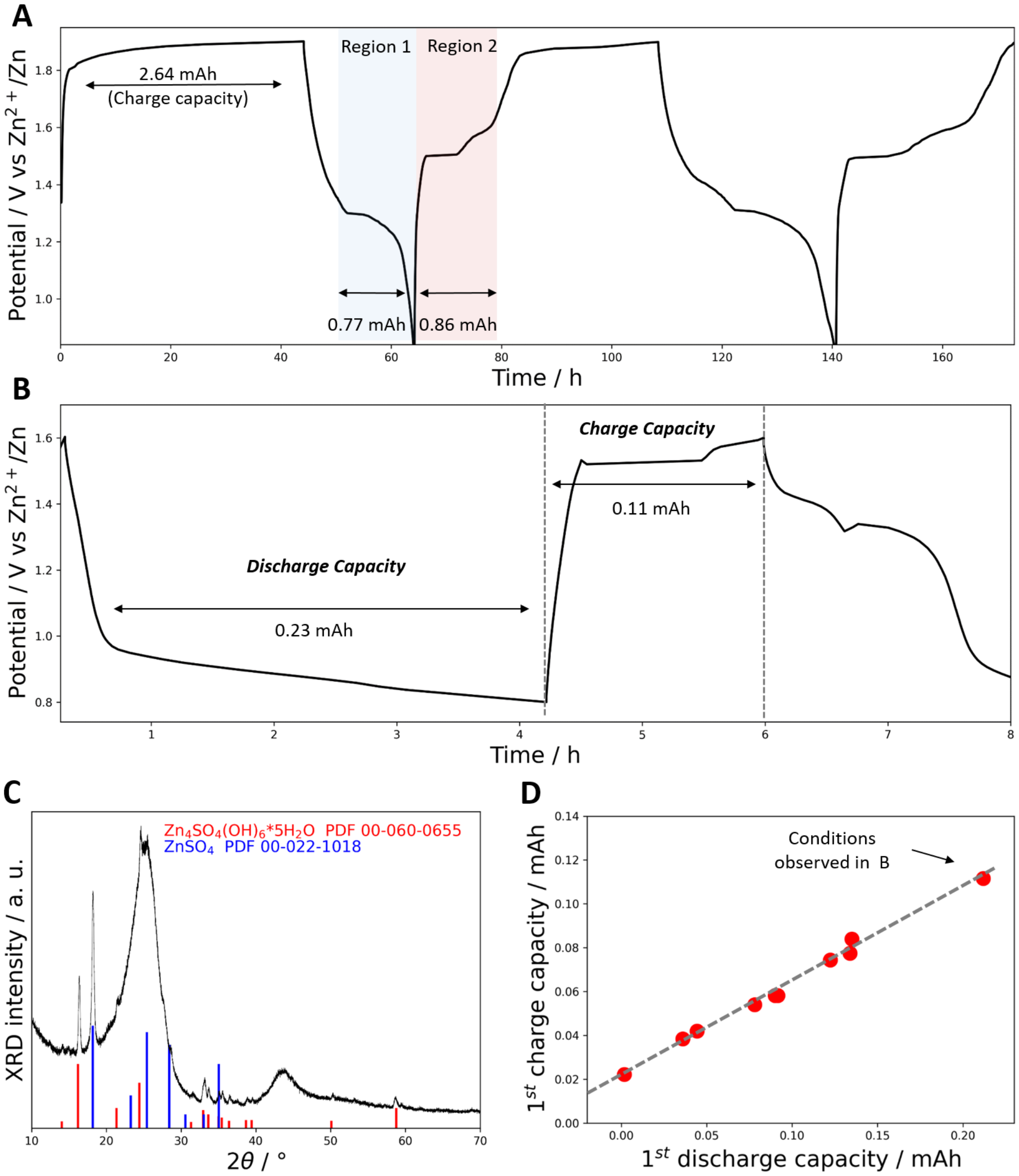

Figure 3. (A) Galvanostatic profile recorded at +/- 60 µA of a C/Zn cell (made of a self-standing carbon powder-based cathode, *i.e.* a mixture of 10 %(w) PTFE and 90 %(w) C_{sp}, and a Zn foil anode) in 700 µL of 2 M $ZnSO_4$ + 0.2 M $MnSO_4$ electrolyte. The cell cycling was started by a charge to induce MnO_2 electrodeposition at the carbon powder-based electrode (electrodeposition time: 44 hours). Temperature: 25°C. **(B)** Same as in A but starting the cell cycling by a discharge. **(C)** XRD patterns (black) of the self-standing carbon powder-based electrode after a galvanostatic discharge in a 2 M $ZnSO_4$ + 0.2 M $MnSO_4$ electrolyte. The reference patterns are given in red and blue. **(D)** First charge capacity as a function of the first discharge capacity for a set of C/Zn cells started by a discharge at different currents (ranging from 10 to 60 µA) and at different voltage cut-offs (between 1 V to 0.65 V) in 700 µL electrolyte (2 M $ZnSO_4$ + 0.2 M $MnSO_4$).

After being deposited, ε-MnO_2 has been discharged at 60 µA (in the same cell, **Figure 3A**), showing the characteristic voltage profile with a voltage hint at 1.3V, delimiting region 1 over which ZHS and probably some ZnMnLDH precipitate as deduced by HAADF-STEM and STEM-EDX (**Figure S21, Supplementary information**). The subsequent charge first shows two stair-case-like plateaus at 1.5V and 1.55V (region 2 in **Figure 3A**), followed by a long plateau at 1.9 V which mirrors the process of the initial charge (identified as ε-MnO_2 electrodeposition and OER). *Ex situ* STEM-EDX and HAADF-STEM studies of the cells stopped at the end of region 2 indicate formation of $Zn_{0.33}MnO_2$ (**Figures S22** and **S23, Supplementary information**). Interestingly, the capacity in region 2 corresponds roughly to the discharge capacity of region 1 (± 10%), thus suggesting that the charge capacity of the electrode below 1.8 V is correlated to the amount of ZHS precipitated over the electrode surface during the first discharge.

To check this point, several C/Zn cells using (2 M $ZnSO_4$ + 0.2 M $MnSO_4$) electrolytes were assembled and started on **discharge** in order to produce zinc hydroxides *in-situ,* since in absence of MnO_2 the reaction on discharge at the carbon black cathode is expected to be the reduction of either dissolved oxygen (*i.e.*, ORR) or protons (*i.e.*, HER). Experimentally, we observe a sloping plateau at 1 V in **Figure 3B**. The cathodic process is proton-consuming, just as the MnO_2 reduction, and similarly triggers the precipitation of ZHS at the cathode surface, as evidenced by XRD (**Figure 3C**). Thereafter, the cell is next charged in a voltage window corresponding to region 2 and we note that the freshly formed ZHS leads to the two stair-case-like plateaus. Additionally, by playing with both the current (10 – 60 µA) and cut-off voltage (1.0 – 0.65 V), we could easily modulate the capacity of the first discharge (mAh) and it turned out that it linearly drives the capacity of the subsequent charge (**Figure 3D**). Altogether, these results evidence that the presence of ZHS – introduced either by starting a C/Zn cell on discharge or through the first discharge of a cell containing MnO_2 – induces the electrodeposition of Mn-oxides at 1.5 V/1.55 V rather than 1.9 V accompanied by the dissolution of ZHS.

Although we proved that the ZHS basic species steer the electrochemical process on charge, it is interesting to determine how a decrease of electrolyte pH can influence the voltage profile of the cell. To change the electrolyte acidity without changing its nature, we have taken advantage of the MnO_2 electrodeposition process to *in-situ* generate protons (eq. 5) in two C/Zn cells charged up to an identical charge of 0.24 mAh but in very different volumes (2 mL *vs.* 300 µL) of the 2 M $ZnSO_4$ + 0.2 M $MnSO_4$ electrolyte. While nearly alike upon charge, the cells behave drastically differently on the following discharge (**Figure 4**). Namely, the cell with a limited amount of electrolyte (300 µL) shows a smooth and continuous voltage decrease (blue curve), indicative of a slow increase of the pH, while the one containing 2 mL of electrolyte exhibits a more conventional profile (green curve), with a fast potential decrease and voltage hint at 1.3 V on discharge, attributed to ZHS precipitation (*vide infra*). Such a behaviour can be explained by higher concentration of H^+ accumulated in the cell of 300 µL at the end of charge (*i.e.*, the pH is lower) compared to the cell of 2 mL (see **Figure 4 caption**). As a result, during discharge these accumulated protons can be more effectively exploited for MnO_2 electrodissolution, leading also to a slower rate of pH decrease. Hence, the voltage hint signing the ZHS precipitation is not observed in the small electrolyte volume. Consistently, when we replace, in a charged cell, the 300 µL of electrolyte by the same amount of fresh electrolyte (removing the H^+ produced during the initial charge), the voltage hint at 1.3 V is recovered (black curve in **Figure 4**). Such observation highlights a strong dependence of the Zn-MnO_2 system on electrolyte volume and composition, especially regarding the source of protons.

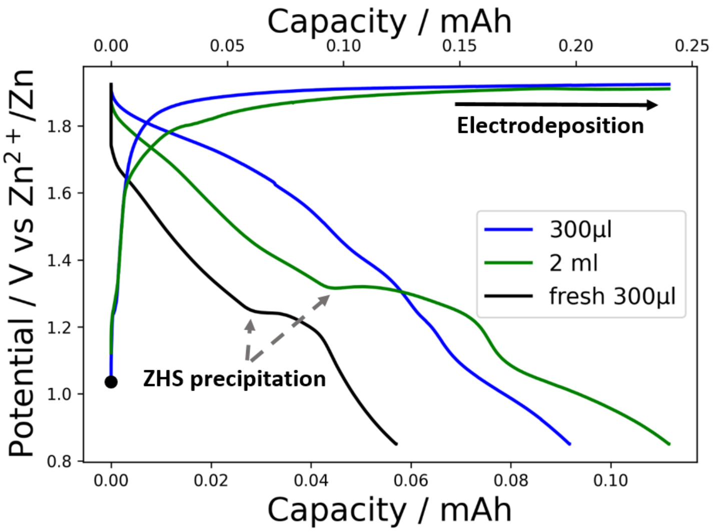

Figure 4. Galvanostatic charge and discharge profile at +/- 30 µA recorded at a C/Zn cell in (blue) 300 µL or (green line) 2 mL of a 2 M $ZnSO_4$ + 0.2 M $MnSO_4$ electrolyte. The black curve is the same experiment as blue curve except that the cell is discharged in fresh 300µl electrolyte. Note that during the galvanostatic charge (performed here at a sufficiently slow rate to be close to the thermodynamic equilibrium) the potential increases less rapidly in the large volume cell (green line), which is indicative of a slower rate of acidification of the bulk electrolyte (the voltage of the cell is indeed directly linked to the pH of the bulk electrolyte through the Nernst equation associated to eq. 5).[38]

3.3. Prospecting the reaction mechanism in Zn-MnO_2 via operando techniques

Operando Raman spectroscopy has been selected to follow the evolution of the Mn-oxides upon cycling since it provides good temporal resolution as well as structural information of poorly crystallized materials.[57] The Raman spectra collected on a carbon PTFE substrate in 2 mL of the 2 M $ZnSO_4$ + 0.2 M $MnSO_4$ electrolyte and their corresponding electrochemical curve are shown in **Figure 5A** (**SI-7 for details**). Initially, the spectrum is nearly flat and with increasing state of charge, the peaks corresponding to ε-MnO_2 appear reaching a maximum intensity at ~2 mAh and remain constant afterwards upon further electrodeposition because the effective Raman penetration depth is exceeded (**Figure 5B**~~)~~. Next, to follow the ε-MnO_2 dissolution and ZHS precipitation, we refreshed the electrolyte solution and observed two different behaviors during the discharge. First, a progressive decrease of the Raman intensity without any frequency shift which denotes the simple dissolution of ε-MnO_2. Once the potential reaches 1.3 V, the ε-MnO_2 signal widens and abruptly decreases in intensity, likely partially masked by the ZHS precipitate (**Figure S25**).[54] Noteworthy, the second charge is marked by the appearance of ε-MnO_2 peaks together with the emergence of a new peak at 650 cm^{-1} indicative of a change in the symmetry of the Mn sites (**Figure 5B**) [55], [58] This suggests, as it has been proposed by TEM study, the growth of an isostructural phase formed upon the second charge (**Figure S26, Supplementary Information**). This does not come as a surprise since the presence of Zn^{2+} into $Zn_{0.33}MnO_2$ induces a Mn^{3+}/Mn^{4+} distribution that changes the symmetry of the MnO_6 octahedra.[59]

In parallel, the reactivity of ZHS has been monitored via *in situ* XRD. An XRD cell was assembled by directly adding ZHS (chemically synthetized beforehand)[60] into the carbon mixture in a 80%(w)/20%(w) ratio (see **SI-8** for experimental details). Upon charge in a 400 µL of 2 M $ZnSO_4$ + 0.2 M $MnSO_4$ electrolyte the cell shows the classical two plateaus at 1.5 V and 1.55 V, while the subsequent discharge curve presents the typical voltage hint attributed to ZHS precipitation. Concomitantly, at an early state of charge,

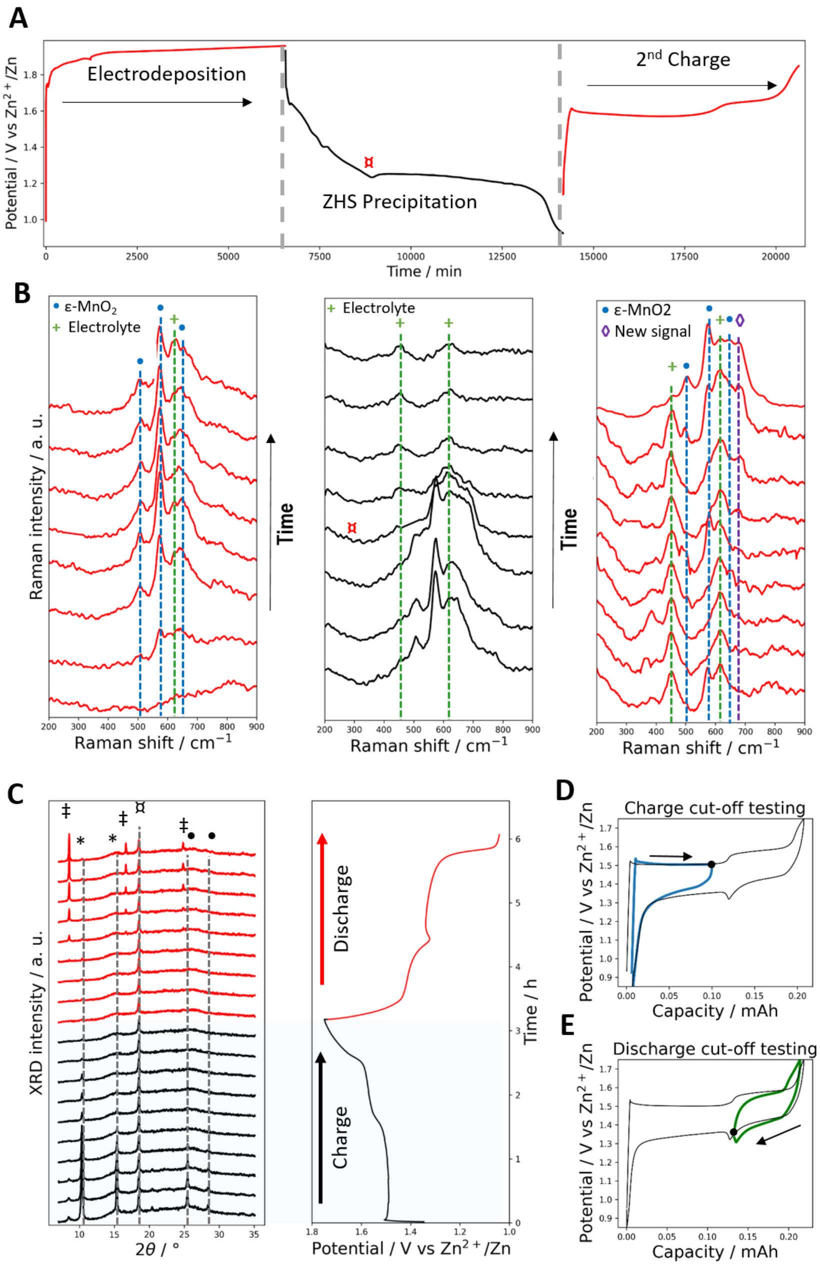

Figure 5. (A) Galvanostatic charge at +/- 60 µAof a C/Zn cell composed of a self-standing electrode (PTFE-C_{sp}) as cathode and a Zn foil as reference and counter electrode in 2 mL of electrolyte (2 mol.L^{-1} $ZnSO_4$ + 0.2 mol.L^{-1} $MnSO_4$), and its subsequent galvanostatic discharge and charge in 2mL of fresh electrolyte at -/+ 60 µA. **(B)** Evolution of the *in situ* Raman spectra acquired using a laser of 514 nm wavelength with collecting times of 802 s for the spectra which represents 0.57 mAh of interval capacity (see **Supplementary Information SI-7 for experimental details**). Noteworthy, we could not trace ZHS evolution by Raman in situ, due to its very low Raman cross section, (**Figure S24, Supplementary Information**). **(C)** Galvanostatic charge and discharge profile and its *in-situ* XRD monitoring of a ZHS-C_{sp}/Zn cell cycled at 10 µA in 2 M $ZnSO_4$ + 0.2 M $MnSO_4$ electrolyte. Attributions: • $ZnSO_4$ $3Zn(OH)_2$. H_2O (*PDF 00-039-0690)*, ⋆ $ZnSO_4$ $3Zn(OH)_2$. $4H_2O$ *(PDF 00-044-0673)*, ‡ *$ZnSO_4$ $3Zn(OH)_2$. $5H_2O$ (PDF 00-039-0688), ¤ Poly(vinylidene fluoride) PDF 00-057-1927).* Synthetic ZHS was synthetized following the protocol Moezzi et al[60] (see Materials and methods). **(D)** First cycle (black line) and Charge voltage cut-off (blue line) of a C/Zn cell wherein the cathode is made of a mixture of 2.4 mg ZHS and 3.6 mg C_{sp}. The cell was cycled (rate: 60 µA) in 2 M $ZnSO_4$ + 0.2 M $MnSO_4$ electrolyte. **(E)** First cycle (black line) and discharge voltage cut-off (green line) recorded under the same experimental conditions than B (except for the cut-off potential).

we identify 4 diffraction peaks corresponding to the synthetic ZHS of the cathodic composite (identified as a mixture of $ZnSO_4$ $3Zn(OH)_2 . 4H_2O$ *and* $ZnSO_4$ $3Zn(OH)_2 . H_2O$ **Figure 5C**). The intensity of the ZHS peaks decreases upon the first charging plateau and the transition to the second charging plateau is marked by a complete intensity loss. Hence, we associate the 1.5 V charging plateau as the main step of ZHS dissolution. During the following discharge process, XRD tracks the appearance of a new ZHS phase (identified as Osakaite, $Zn_4(OH)_6SO_4.5H_2O$) where the voltage hint occurs, thus confirming its attribution to a phase nucleation and growth process.[39], [40], [61]

By limiting the charge to the first plateau so that some synthetic ZHS remains at the cathode (**Figure 5D**), we do no longer observe the voltage hint in the following discharge curve, implying that the inflexion point observed on charge (delimiting the 1.5 V and 1.55 V plateaus) governs the appearance of the voltage hint on discharge. Similarly, we can avoid the voltage hint associated to ZHS precipitation (**Figure 5E**) by first full charge of the electrode and then limiting the following discharge before the voltage hint~~,~~ hence implying that the first discharge plateau is related to the charge process at 1.55 V. This demonstrates that there are two equilibriums of different nature in the system, likely resulting from the ZHS dissolution mechanism.

At this stage, to grasp for further insights into the interfacial processes, we performed *in situ* electrochemical quartz crystal microbalance (EQCM) experiments using a laboratory-designed EQCM hardware with Au-patterned quartz crystals acting as the working electrode (**SI-9 for details**). First, we examined the microbalance frequency profiles induced by the electrochemical deposition of MnO_2 in the presence of an aqueous buffered electrolyte made of 1 M sodium acetate + 0.1 M $MnCl_2$ (pH 5), which acts as a proton source while keeping the pH constant.[37], [38] During the electrochemical deposition of MnO_2 at 12 µA for 34 min in 4 mL acetate buffer, there is, in line with previous reports,[62], [63] a linear increase of the electrode mass up to 24.6 µg throughout a 1.56 V plateau (*vs*. Zn^{2+}/Zn) (**Figure S29**). The mass per electron was calculated as 140 $g.mol^{-1}$ by combining the Sauerbrey equation and the Faraday law ($\frac{M}{z} = F\frac{\Delta m}{\Delta Q} = -FC_f\frac{\Delta f}{\Delta Q}$), assuming a 1.7-electron oxidation process.[62] It was attributed to $MnO_2{\cdot}nH_2O$, where here $n = 3$ (considering the molar mass of MnO_2 equals to 87 $g.mol^{-1}$). Note that such charging protocol was used for all the EQCM experiments hereafter.

Upon the subsequent discharge at a current of -3 µA, the frequency linearly increases along the well-defined plateau at 1.5 V, thus reflecting a steady loss of mass as expected for an electrodissolution process at a constant rate (**Figure 6A**). Such process is accompanied by little changes in the motional resistance (ΔR_m of ~15 Ω, **Figure S30, Supplementary Information**), indicating that electrodissolution induces small variations of the viscosity and density at the MnO_2 film/electrolyte interface and/or of the viscoelastic properties of the MnO_2 film itself. Pushing the reduction further, the frequency still increases at the same constant rate while the galvanostatic curve goes through a second short plateau at 1.35 V, which might be indicative of a fraction of MnO_2 that is more resistive against dissolution. Finally, we recover ~88% of the charge capacity by the electrodissolution process.

For sake of completion, the electrodissolution process has also been studied in a sulphate-based electrolyte by EQCM (**Figure 6B**). At the early state of discharge (Region I), the electrochemical dissolution of MnO_2 is accompanied by an unexpected slight frequency decrease (increase in mass) which occurs with very low changes in motional resistance, R_m (less than 10 Ω in Region I **Figure S31, Supplementary Information**), and a small $\Delta R_m/\Delta f$ ratio, hence suggesting that no precipitate is formed in Region I. This led us to assume that the mass loss associated to MnO_2 electrodissolution is here counterbalanced by some physical phenomenon that could be related to locally generated deprotonated

Zn^{2+} complexes (as proposed in eq. 2). Indeed, such complexes are prone to condensation,[64], [65] leading to the formation of soluble polynuclear entities of higher molecular sizes and lower mobility,[66] which might accumulate at the electrode/electrolyte interface as a result of an imbalance between their production rate and loss by mass transport *(i.e.*, by diffusion into the bulk electrolyte). Note that the penetration depth of the acoustic wave in our EQCM measurements (9 MHz, fundamental frequency) is 189 nm,[67]–[69] thus allowing to detect the accumulation of such soluble species at the vicinity of the electrode. Subsequently, zero-charged mono- or polynuclear precursors will nucleate into a solid phase once their solubility limit is reached, leading to the precipitation of hydroxides such as ZHS. A similar process of nucleation/growth has been proposed for LiS composite in lithium sulphur batteries.[70]

Turning to Region II (**Figure 6B**), there is a huge frequency decrease that occurs conjointly with substantial changes in the motional resistance, R_m (**Figure S31, Supplementary Information**), that can be assuredly ascribed to the precipitation of ZHS since it appears synchronously with the voltage hint at 1.3 V. Moreover, the change in R_m is indicative of an increase of the interface's density and viscosity so that the acoustic wave has more difficulty crossing it. In such cases, the Sauerbrey equation is invalid, but the R_m can be used as a qualitative indicator of ZHS formation.[61], [67], [68] Such a formation was straightforwardly confirmed by FEG-SEM images (**Figure S32, Supplementary Information**) that show a dramatic change in morphology with particles appearing on the surface after the potential bend with a compositional Zn:S ratio close to 3:1 (likely corresponding to a Zn-layered double hydroxide phase with entrapped SO_4^{2-}ions). Altogether, these results indicate that the mechanistic pertaining to the functioning of the Zn-MnO_2 cells is strongly influenced by the nature of the electrolyte with the buffer acetate being somewhat the model media to eliminate pH gradients.

Next, to better understand the nucleation-growth process of ZHS in sulfate-based electrolytes in Zn-MnO_2 cells, we explore the role of cycling either at a varying or constant C rate. **Figure 6C** shows the discharge at different rates (0.2 C, 0.4 C and 1.6 C) of three cells loaded with freshly deposited 24.6 μg MnO_2. The cells show nearly the same discharge capacity and an abrupt frequency decrease when the voltage hint appears. Note that the frequency response (in Region I) is negative for high/medium C-rates indicating mass gains (**Figure 6D**) while the frequency response is positive (mass losses) for low C-rates (**Figure 6E**). This suggests a larger accumulation of soluble basic species at the interface when high rates are used, in agreement with our assumption that slow discharge generates less mobile polynuclear species through condensation. Moreover, we note that the voltage hint associated to hydroxide precipitation appears earlier as the current increases (**Figure 6C**), further confirming that an increase in current density promotes accumulation of such species and hence the earlier precipitation of ZHS.

Lastly, we fix the C-rate at 0.4C for three cells with different MnO_2 loading (*i.e.,* 18.45 μg, 24.6 μg and 36.9 μg), in order to establish the flux of basic soluble species produced at the MnO_2/electrolyte interface and thus snapshot the time when the precipitation of ZHS starts. **Figure 6F** shows that the voltage hint occurs at the same time in the three cases which corresponds to a gravimetric capacity of 136 mAh/g. Moreover, the three cells show similar frequency decreases in Region I, indicating that the ZHS precipitation dynamics is the same **Figure 6G-H**. However, there is some limit to this trend when the current becomes very low (small loadings at same C-rate) so that the frequency in Region I increases (**Figure S33, Supplementary Information**). This is indicative of a regime with less interfacial accumulation of basic soluble species that induces a delay in the precipitation of ZHS occurring at 175 mAh/g. Finally, the length of the second discharge plateau (Region II) decreases with the MnO_2 loading (**Figure 6F**) suggesting that the faster the precipitation of ZHS, the greater the chance of blocking the discharge process as suggested by the difference in the slope of the frequency plot (calculated at the

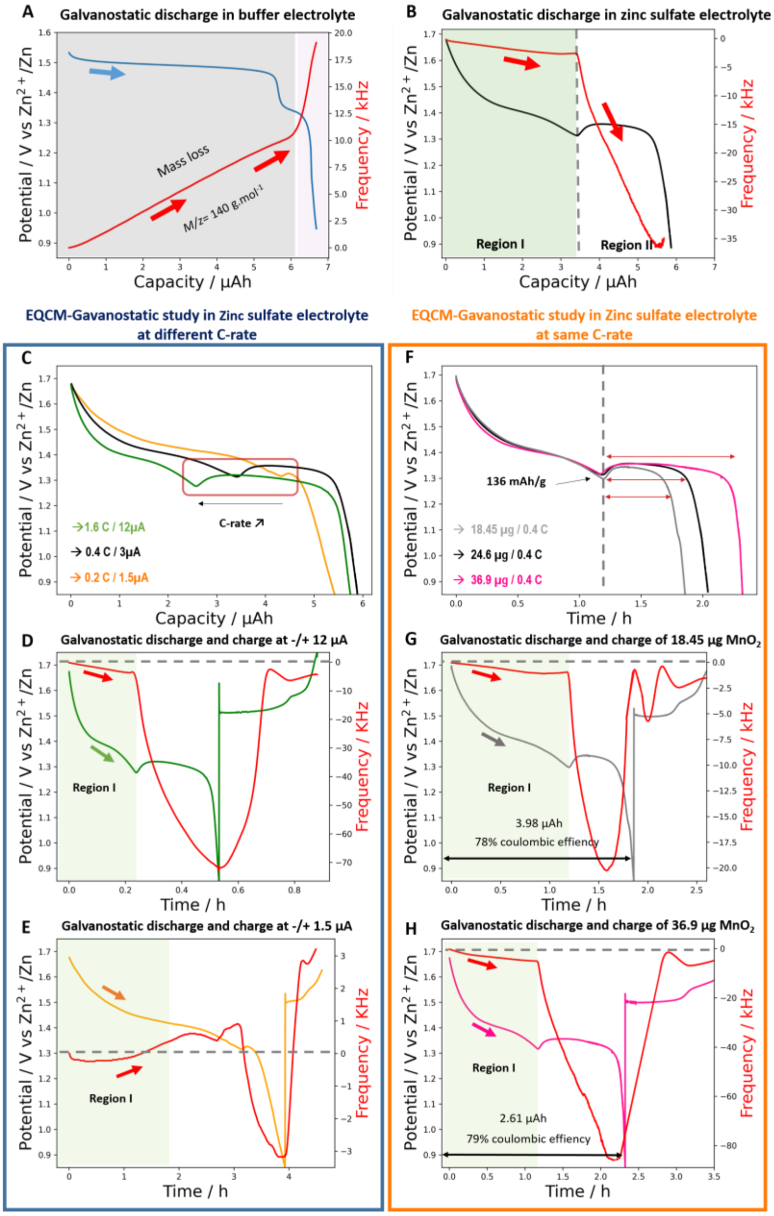

Figure 6. (A) (blue curve) Galvanostatic discharge profile at -3 µA recorded at a carbon-coated Au-quartz resonator over which was electrodeposited 24.6 µg MnO_2 and (red curve) the corresponding frequency variation during MnO_2 electrodissolution in a 4mL acetate buffer (1 M acetate buffer + 0.2 M $MnCl_2$) of pH 5. A Pt and Hg/Hg_2SO_4 were used as counter and reference electrodes, respectively. **(B)** (black curve) Same as in A but in a 4 mL of 2 M $ZnSO_4$ + 0.2 M $MnSO_4$ electrolyte and (red curve) the corresponding frequency response. **(C)** Galvanostatic discharge of 24.6µg MnO_2 at -1.5µA (orange curve), -3µA (black curve) and -12µA (green curve) corresponding to 0.2C, 0.4C and 1.6C, respectively. The C-rates were calculated following the equation: C= I/Q_c where I corresponds to the applied current (in µA) and Q_c to the capacity (in µAh) used to electrodeposit 24.6 µg MnO_2. **(D)** Galvanostatic discharge/charge (green curve) and frequency variation (red curve) of 24.6µg MnO_2 cell at ±12µA / 1.6 C. **(E)** Galvanostatic discharge/charge (orange curve) and frequency variation (red curve) of 24.6µg MnO_2 cell at ±1.5µA / 0.4 C. **(F)** Galvanostatic discharge *vs* time of 18.45 µg MnO_2 (gray curve), 24.6 µg (black curve) and 36.9 µg MnO_2 (pink curve) at 0.4 C (0.12 µA/µg MnO_2). **(G)** Galvanostatic discharge *vs* gravimetric capacity (gray curve) and frequency variation (red curve) of 18.45 µg MnO_2. **(H)** Galvanostatic discharge/charge (pink curve) and frequency variation (red curve) of 36.9 µg MnO_2 cell. Note the irregular behaviour of the frequency at the end of the discharge, which sometimes starts to increase (6G and 6H). This behaviour could reflect a limited mechanical stability of the ZHS bulk deposit, but without a clear trend being discernible.

beginning of the nucleation process **Figure S34, Supplementary Information**).Such conclusion is in line with literature reports showing limited capacities at high C rates.[16], [35]

Regarding the subsequent charges, all the voltage profiles commonly exhibit the typical two plateaus while the frequency curves follow the same trend. The sharp increase of frequency is associated to the dissolution of ZHS forced by the electrochemical process. Moreover, we note a high $\Delta R_m/\Delta f$ ratio all along the first plateau signing the presence of ZHS (in agreement with *in situ* XRD measurements in **Figure 5C**). The transition to the second charging plateau is marked by a drastic decrease of the motional resistance, which returns to its initial value (**Figure S31, Supplementary Information**), thus confirming that the ZHS layer is almost inexistent at this point. Surprisingly, the frequency remains almost constant all over the second plateau while MnO_2 is deposited. This suggests again the formation of soluble basic species from the partial dissolution/hydrolysis of ZHS during the MnO_2 electrodeposition, which due to their poor mobility remain close to the electrode surface and thereby provide an extra buffering effect.

Altogether, the results that are observed upon cycling provide the irrevocable proof that the voltage hint is associated to the precipitation of ZHS with the evidence of two reversible processes dealing with either solid ZHS or soluble basic species, with the former already detected by XRD (**Figure 5C**). Next, we take benefit from such a fundamental insight to improve aqueous Zn-MnO_2 cells via the selection of electrode composites based on specific additives.

3.4. Improving the energy density of Zn-MnO_2 through cathodic composites

Knowing that most of the side reactions involved in the system (such as water oxidation and zinc corrosion) become predominant when the pH is not controlled during cycling, we focused our attention on the equilibrium of ZHS, which, through its buffering properties, significantly reduces pH changes. Thus, we studied the effect of ZHS on the cycling performances of Zn-MnO_2 batteries by adding solid ZHS chemically synthetized (identified in **Figure 5C**) to the carbon cathode mixture in place of MnO_2 as has been adopted in previous works.[24], [54] The cell was charged against a Zn foil in 300 µL of 2 M $ZnSO_4$ + 0.2 M $MnSO_4$ electrolyte, at a potential of 1.75 V to avoid OER, reporting a columbic efficiency of ~1.6 electrons per Mn^{2+} ion according to ICP quantification (see **Supplementary Information SI-10** for experimental details). Interestingly, by increasing the amount of ZHS, we succeeded in scaling up the capacity of the system (**Figure 7A**), echoing our previous experiments with *in-situ* formation of ZHS (**Figure 3D**). Both charge and discharge show that the amplitudes of the two plateaus increase with the initial mass of solid ZHS, and by the same magnitude, hence, the galvanostatic profiles stay almost unchanged (**Figure 7B**). Finally, the cathode delivers a specific discharge capacity of 103 mAh/g_{ZHS} that is relatively lower than the gravimetric capacity reported by Zhao et al. (123 mAh/g_{ZHS}).[24] Such differences find its ground in the hydration of the initial ZHS additive. However, the benefit of adding ZHS in lowering the electrodeposition voltage of MnO_2 and by the same token avoiding OER, is negated by its penalty imposed on the energy density of "ZHS-C/Zn cells" with respect to conventional MnO_2/Zn cells due to its low weight content in OH^- (around 22% in $Zn_4(OH)_6SO_4$). This has prompted us to replace ZHS by other poorly soluble metal ions-based hydroxides/oxides, with lower molecular mass. Along that line, we selected three compounds: ZnO, $La(OH)_3$ and $Mg(OH)_2$, which could also be hydrolyzed by the protons released during the MnO_2 electrodeposition (see reactions below), thus ensuring a buffering effect. According to their weight content in OH^-, the gravimetric buffering efficiency is expected to decrease by a factor 2.2 from $Mg(OH)_2$ (59%) to $La(OH)_3$ (27%) (see **table S5, Supplementary information)**. Furthermore, depending on the Brønsted acidity of their aquo soluble metal ions complexes (see reactions below), they can also act

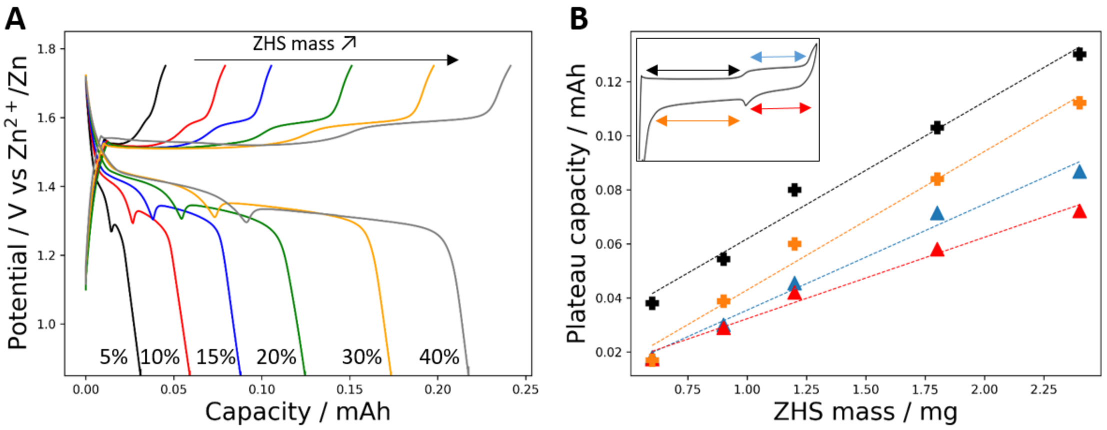

Figure 7. (A) Galvanostatic charge and discharge profiles at a constant current of +/- 60 µA of C-ZHS/Zn cells containing different amounts of ZHS (0.6 to 2.4 mg). **(B)** Plateau capacity (extracted from A) as a function of the added ZHS mass in the cathode mixture.

as proton donor during the following discharge, and thus be part of the basic species that accumulate/precipitate at the electrode.[50], [71], [72]

(6) $ZnO_{(s)} + 2\,H^+_{(aq)} + 5\,H_2O \rightleftarrows [Zn(H_2O)_6]^{2+}$ $\quad$ $pK_s = 17$ (in water)
(7) $[Zn(H_2O)_6]^{2+} \rightleftarrows [Zn(OH)(H_2O)_5]^{+} + H^+_{(aq)}$ $\quad$ $pK_{a1} = 9$

(8) $La(OH)_{3\,(s)} + 3\,H^+_{(aq)} + 3\,H_2O \rightleftarrows [La(H_2O)_6]^{3+}$ $\quad$ $pK_s = 18.9$ (in water)
(9) $[La(H_2O)_6]^{3+} \rightleftarrows [La(OH)(H_2O)_5]^{2+} + H^+_{(aq)}$ $\quad$ $pK_{a1} = 8.5$

(10) $Mg(OH)_{2\,(s)} + 2\,H^+_{(aq)} + 4\,H_2O \rightleftarrows [Mg(H_2O)_6]^{2+}$ $\quad$ $pK_s = 11$ (in water)
(11) $[Mg(H_2O)_6]^{2+} \rightleftarrows [Mg(OH)(H_2O)_5]^{+} + H^+_{(aq)}$ $\quad$ $pK_{a1} = 11.4$

To confirm the feasibility of ZnO, $La(OH)_3$ and $Mg(OH)_2$ to be employed as buffer species, we first characterized their dissolution/precipitations kinetics by performing acid-base titrations in 2 M $ZnSO_4$ (**Figure S35, Supplementary Information**). As expected, the solids are dissolved easily by the addition of an acidic solution (similar behavior observed for ZHS), at a quite stable pH ranging from 5.5 to 6. They are thus all suitable to successfully replace ZHS. Subsequently, the electrochemical performances of ZnO, $La(OH)_3$ and $Mg(OH)_2$ were tested in 2-electrode Swagelok cells. For this study, the mass of the positive electrode was set at 6 mg with an additive mass ratio of 20% ZnO, 20% $La(OH)_3$ and 10% $Mg(OH)_2$ (see **Supplementary Information SI-11** for experimental details). The cells were cycled against Zn in 200 µL of electrolyte (2 M $ZnSO_4$ + 0.2 M $MnSO_4$) in a potential range of 0.75 V-1.75 V and the current density was normalized at 0.55 A/g_{OH} (**Figure 8**). Note that this electrolyte contains 40 µmol of Mn^{2+}, and therefore allows a maximum charge capacity of 1.8 mAh (assuming a 1.7-electron per Mn^{2+} oxidation process).

Interestingly, in the cells containing ZnO and $Mg(OH)_2$, the electrodeposition mirrors the electrochemical profile spotted in ZHS-containing cells, with two well-defined plateaus implying that the electrochemical proton-coupled process occurs without significant electrolyte pH change. The similarity with ZHS is not so surprising and confirms that it is not necessary for the basic additive to initially contain Zn^{2+} ions to allow for the cell to be charged at low potentials. Moreover, almost 98% of the charge capacity is recovered on discharge, indicating a highly reversible process. Concerning the $La(OH)_3$-C/Zn cell, the typical staircase charging plateaus morph into a sloping plateau (**Figure 8C**), which reflects a less effective buffering effect. Nevertheless, the system recovers the typical profile in the subsequent charge/discharge cycle. In the following discharge, the three additives show a nucleation peak at 1.3 V from the first discharge. The peak cannot be related to the re-crystallization of ZnO, $La(OH)_3$ or $Mg(OH)_2$ since it would not occur at the same potential (different pH ranges of existence), hence, the additive buffer effect exclusively intervenes during the first charge.

Thereafter, we proceed to assemble several cells with different masses of ZnO, $La(OH)_3$ and $Mg(OH)_2$ (as we did for ZHS), by varying the carbon/additive ratio in the 6 mg positive electrode and keeping the cycling current at 60 µA. The galvanostatic profiles are shown in **Figure S36-S38, Supplementary Information**. As expected, the increase of the additive mass in the cathode mixture leads to an increase of the overall capacity. However, to compare the buffer capabilities between the different compounds, only the equivalent amounts of OH^- were considered instead of the amount of additive (since the stoichiometry of the additives are different, see eqs 5-7). Thus, by plotting the number of electrons exchanged during the first charge as a function of the equivalent number of OH^- ions in the additive, we obtained a linear relationship with an average slope of 0.42 e^-/OH^- for all basic additives. Such observation is close to the 0.5 value expected for Mn^{2+} oxidation (*i.e.*, 2 H^+ for each 1 e^- exchanged). This fact greatly supports our ICP quantification and highlights the efficient and similar *in-situ* buffering effect of the tested additives.

Assuming that the buffer capabilities are equivalent for the three additives, we proceed to compare them in terms of specific capacity and long cycling performances (**Figure 8D**). Unfortunately, the only additive able to increase the energy density with respect to Zn-MnO_2 cell (cell cycled under similar conditions, **Figure S39, Supplementary information**) is $Mg(OH)_2$, which delivers a gravimetric capacity of 412 mAh/g.

On the other hand, looking at the long cycling performances of these additives (**Figure 8D**), we can observe that the stability is sensibly higher when $Mg(OH)_2$ and $La(OH)_3$ are used. At this stage, one could wonder what is so specific about them when they are placed in the 2 M $ZnSO_4$ + 0.2 M $MnSO_4$ electrolyte. One explanation could rely in the acidity of $[Zn(H_2O)_6]^{2+}$ (initially present in the electrolyte) that implies its partial deprotonation in the presence of basic additives such as $La(OH)_3$ and $Mg(OH)_2$, inducing the *in-situ* formation of zinc-based hydroxides species.[73]. Another could be nested in the specific role of solid additives such as $La(OH)_3$ and $Mg(OH)_2$) during the first electrodeposition process that could lower the contribution of $Zn_{0.33}MnO_2$, hence by changing the nature of the electrodeposited film, we could change the electrochemical performances of the system. The latter is supported by the fact that ZHS-C/Zn cells cycled in electrolytes containing a small concentration of 0.07 M $La_2(SO_4)_3$ or 0.07 M $MgSO_4$ do not exhibit improvement of their cyclability as opposed to those assembled with solid additives as part of the electrodes (**Figure S40, Supplementary information**).

Although offering positive attributes, we must state that the use of additive does not simplify the system as all the processes still strongly depend on the experimental cycling conditions. For instance, by simply changing the additive/ C_{sp} mass ratio or the amount of electrolyte, we could observe that the cycling performances differ considerably (**Figure S36-S38, Supplementary Information**). Hence, the need to optimize the operational conditions for these additives (as we have done here **Figure 8D**), for which we obtained a significantly improved cyclability as compared to literature while using low C-rate.[54] Accordingly, caution has to be exercised when comparing the performances of cathodic additives.

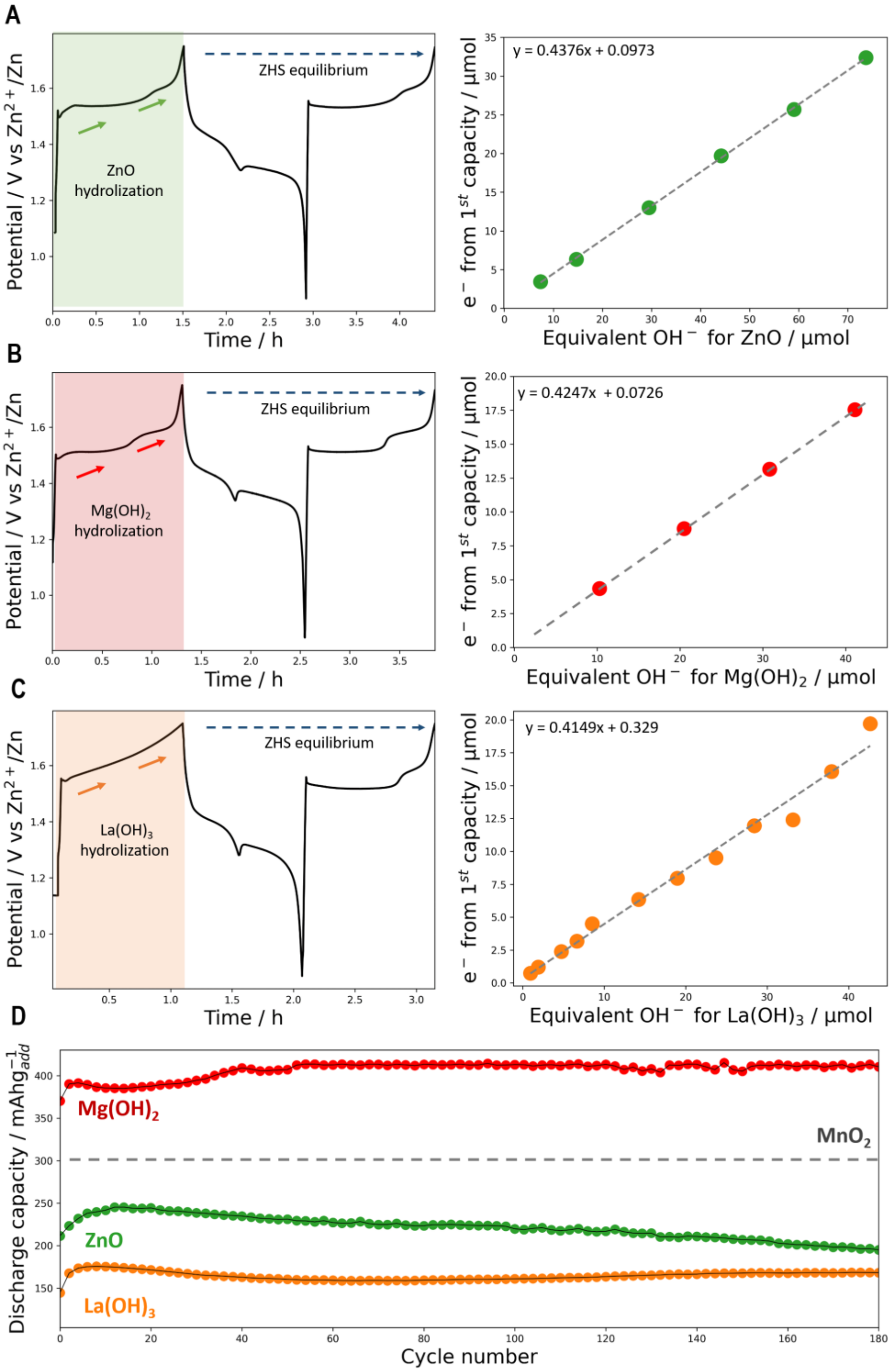

Figure 8. (left) Galvanostatic profiles *vs* time of **(A)** 20% ZnO-C/Zn cell, **(B)** 10% $Mg(OH)_2$-C/Zn cell and **(C)** 20% $La(OH)_3$-C/Zn cell, in 200µL of electrolyte (2 M $ZnSO_4$ + 0.2 M $MnSO_4$) at a current density of 0.55 A/g_{OH-}. **(right)** Amounts of hydroxides added as a function of electrons (µmol) extracted from the 1st charge capacity (each point represents a cell with a different additive mass). The current density of 0.55 A/g_{OH-} were established by using the following equation: $g_{OH-} = n_{additive} \times M_{OH-} \times R$, where $n_{additive}$ corresponds to the amount of additive (mol), M is the molecular mass of the additive (g/mol) and R the number of OH^- contained in the chemical formula of each additive. **(D)** Cycle performance of $Mg(OH)_2$-C/Zn cell, $La(OH)_3$-C/Zn cell and ZnO-C/Zn cell, in 200µL of electrolyte (2 M $ZnSO_4$ + 0.2 M $MnSO_4$) at a current density of 0.55 A/g_{OH-}.

4. Discussion-Conclusions

We have focused on studying the underlying science beyond the rechargeability of Zn-MnO_2 batteries *via* combining solution chemistry considerations and experimental methods, including structural and electrochemical analyses, while bearing in mind early reports and recent advances. A survey of various parameters enlisting the (*i*) nature, composition of the C-MnO_2 positive electrode; (*ii*) composition and volume of the electrolyte, and (*iii*) presence of solid basic additives and their effects on the electrochemistry of Zn-MnO_2 cells have been studied for different sweeping voltages and cycling currents.

Independently of the presence or absence of MnO_2 in the pristine positive electrode, we found that the voltage-composition profiles, once the first cycle achieved, always show the same electrochemical fingerprint response, namely two voltage plateaus on charge and a voltage hint on discharge. We unambiguously demonstrate the latter to be linked to the sudden precipitation of ZHS that conjointly occurs with the electrodissolution of MnO_2.

From *ex-situ* SAED, HAADF-STEM, EDX, and EELS analysis of the charged and discharged cathode, we confirmed the presence of ZHS at the end of the discharge step, and evidenced the accumulation of a new $Zn_{0.33}MnO_2$ phase upon cycling. Which could nucleate from an amorphous one. By adding ZHS (either *in-situ* or *ex-situ*) to the initial composite electrode, we demonstrated its key role in lowering the MnO_2 deposit voltage at near 1.5 V on charge, rather than >1.8 V in absence of ZHS, hence directly acting on the pH of the cell and the competitive OER (only observed under strongly acidic conditions). This lead us to the selections of cathodic basic additives such as $Mg(OH)_2$ or $La(OH)_3$ that result in an enhanced capacity retention of Zn-MnO_2.

From *in-situ* Raman, XRD as well as EQCM measurements, we confirmed the precipitation of ZHS concomitant to the voltage hint during the galvanostatic discharge, and that its presence as a precipitate is associated to the first plateau at 1.5 V observed upon charge. All along this first plateau, the local heterogeneous ZHS/Zn^{2+} electrolyte buffers the pH at a highly stable value of 5.2, resulting into a highly stable electrodeposition voltage. We also showed that the transition from the first to the second charge plateau is related to the disappearance of solid ZHS at the electrode interface. Still, the quite stable potential of the second plateau signs a stable local pH and thus, indirectly, the presence of some basic species to neutralize the protons released during the charge and avoid significant acidification of the electrolyte (which is only observed at the end of the charge, once the voltage shows a sudden rise up to 1.8-1.9 V). The presence of basic soluble species in the vicinity of the electrode during the early stage of the discharge (*i,e,.* before the voltage hint) was confirmed by EQCM, suggesting that the complex sol-gel chemistry of metal cations is likely at work prior/after ZHS precipitation/dissolution.

Although our study provides greater insights on the fundamental correlations between ZHS precipitation, MnO_2 electro-dissolution, and local interfacial pH, there are still remaining unclarified questions. A first one, regards the absence of a clear voltage hint during the first discharge whatever type of MnO_2 is used, while ZHS is detected from ex-situ electrode characterization, and the voltage hint omnipresent in all data from the second cycle onward. A possible explanation can be rooted in pH variation triggered by the pristine material. Indeed, since the mechanism relies on electrodissolution/electrodeposition; one could anticipate the dispersion of the active material within the composite electrode to differ prior and after the first cycle, leading to different space-time distribution of soluble basic species production and thus ZHS precipitation.

Secondly, according to literature reports, the need to add $MnSO_4$ is mandatory for achieving good cycling performances. We challenge this statement since we observed good cycling performance for Zn-

MnO_2 cells using 40 mg of MnO_2 and 200µl of Mn-free $ZnSO_4$ electrolyte. Noteworthy; with this weight to volume ratio, the amount of Mn^{2+} produced during the reduction leads to an electrolyte having a concentration in Mn^{2+} of 0.37 M that far exceeds the 0.2 M threshold reported in the literature, hence highlighting further the importance of the electrolyte volume relative to the weight of active material and the risk of issuing general rules.

Finally, we have spotted as many other groups in the past, the presence of some amount of Zn in the charged and discharged samples, with a systematically lower amount for the latter. Although its presence is well established, its role has been quite controversial. Initially it was wrongly believed that Zn^{2+} reversibly insert into MnO_2 leading to the hastily denomination of Zn-ion batteries. Obviously, the greater amount of Zn in the charged sample revokes this assumption as Zn^{2+} ion should intercalate on reduction. In contrast, the feasibility of stabilizing metal-ion doped MnO_2 is quite classical in the field of electrodepostion,[74] and this happens if the compound to be formed, herein $Zn_{0.33}MnO_2$ has a free energy of formation lower than that of its separate components that is ZnO and MnO_2 if the deposition takes place under conditions close to thermodynamic equilibrium. Once formed such a phase will go through an electrodissolution process upon discharge while reforming on the subsequent charge, with its observed accumulation after 10 cycles suggesting only partial reversibility, hence explaining somewhat the capacity decay.

In conclusion these observations and unanswered questions further highlight the complexity of the rechargeable Zn-MnO_2 chemistry and put somewhat in perspective the few decades of research that went in moving from saline to primary alkaline batteries. Such a complexity is intrinsic to battery systems having the electrolyte being an active part of the cell redox chemistry, alike Pb-acid batteries whose chemistry after nearly 200 years of research is less understood than that of the 30 years old Li-ion chemistry. Let's hope that the reverse journey of going from primary alkaline to rechargeable saline batteries using a mild acidic electrolyte will be shorter. We hope that the additional knowledge and findings provided by this work will contribute in shortening the practical development of such rechargeable Zn-MnO_2 chemistry.

5. Acknowledgment

This work is financially supported by the European Research Council (ERC) (no. FP/2014/ERC; grant project no. 670116-ARPEMA). The authors thank M. Courty (Laboratoire de Réactivité et Chimie des Solides, Amiens, France) for BET measurements, Ronan Chometon and Louis Godeffroy for the SEM imaging. Access to transmission electron microscopy equipment is provided by AICF of Skoltech

6. References

[1] M. Armand and J.-M. Tarascon, "Building better batteries M. Armand and J.-M. Tarascon Researchers," *Sustain. Energy Fuels*, vol. 3, no. 1, pp. 280–291, 2019.

[2] M. Luo, W. Sun, B. Bin Xu, H. Pan, and Y. Jiang, "Interface Engineering of Air Electrocatalysts for Rechargeable Zinc–Air Batteries," *Adv. Energy Mater.*, vol. 11, no. 4, pp. 1–14, 2021, doi: 10.1002/aenm.202002762.

[3] J. M. Tarascon, "Na-ion versus Li-ion Batteries: Complementarity Rather than Competitiveness," *Joule*, vol. 4, no. 8, pp. 1616–1620, 2020, doi: 10.1016/j.joule.2020.06.003.

[4] J. O. G. Posada *et al.*, "Aqueous batteries as grid scale energy storage solutions," *Renew. Sustain. Energy Rev.*, vol. 68, pp. 1174–1182, 2017, doi: 10.1016/j.rser.2016.02.024.

[5] Y. Shen *et al.*, "Water-in-salt electrolyte for safe and high-energy aqueous battery," *Energy Storage Mater.*, vol. 34, no. October 2020, pp. 461–474, 2021, doi: 10.1016/j.ensm.2020.10.011.

[6] L. Droguet, A. Grimaud, O. Fontaine, and J. M. Tarascon, "Water-in-Salt Electrolyte (WiSE) for Aqueous Batteries: A Long Way to Practicality," *Adv. Energy Mater.*, vol. 10, no. 43, pp. 1–14, 2020, doi: 10.1002/aenm.202002440.

[7] B. Lee, C. S. Yoon, H. R. Lee, K. Y. Chung, B. W. Cho, and S. H. Oh, "Electrochemically-induced reversible transition from the tunneled to layered polymorphs of manganese dioxide," *Sci. Rep.*, vol. 4, pp. 1–8, 2014, doi:

10.1038/srep06066.

[8] M. H. Alfaruqi *et al.*, “Electrochemically induced structural transformation in a γ-MnO2 cathode of a high capacity zinc-ion battery system,” *Chem. Mater.*, vol. 27, no. 10, pp. 3609–3620, 2015, doi: 10.1021/cm504717p.

[9] W. J. Wruck, B. Reichman, K. R. Bullock, and W. Kao, “Rechargeable Zn - MnO 2 Alkaline Batteries Rechargeable Zn-MnO2 Alkaline Batteries,” *J. Electrochem. Soc.*, vol. 138, no. 12, pp. 3560–3567, 1991.

[10] K. K. Y. Sharma, A. Haynes, L. Binder, “The Effect of the Amount of Electrolyte in the Anode Gel on the Rechargeability of Alkaline Manganese Dioxide-Zinc Cells,” *J. Power Sources*, vol. 27, pp. 145–153, 1989.

[11] L. Binder, W. Odar, and K. Kordesch, “A study of rechargeable zinc electrodes for alkaline cells requiring anodic limitation,” *J. Power Sources*, vol. 6, no. 3, pp. 271–289, 1981, doi: 10.1016/0378-7753(81)80032-8.

[12] E. Faegh *et al.*, “ Understanding the Dynamics of Primary Zn-MnO 2 Alkaline Battery Gassing with Operando Visualization and Pressure Cells ,” *J. Electrochem. Soc.*, vol. 165, no. 11, pp. A2528–A2535, 2018, doi: 10.1149/2.0321811jes.

[13] D. Linden, *Linden’s Handbook of Batteries, Chapter 8 : Zinc-Carbon Batteries (Lechanché and Zinc Chloride Cell Systems)*, Third edit. .

[14] T. Yamamoto and T. Shoji, “Rechargeable ZnlZnSO, IMnO+pe Cells,” *Inorganica Chim. Acta*, vol. 117, pp. 27–28, 1986.

[15] C. Xu, B. Li, H. Du, and F. Kang, “Energetic Zinc Ion Chemistry: The Rechargeable Zinc Ion Battery,” *Angew. Chemie*, vol. 124, no. 4, pp. 957–959, 2012, doi: 10.1002/ange.201106307.

[16] H. Pan *et al.*, “Reversible aqueous zinc/manganese oxide energy storage from conversion reactions,” *Nat. Energy*, vol. 1, no. April, pp. 1–7, 2016, doi: 10.1038/nenergy.2016.39.

[17] D. Wang *et al.*, “A Superior δ-MnO2 Cathode and a Self-Healing Zn-δ-MnO2 Battery,” *ACS Nano*, vol. 13, no. 9, pp. 10643–10652, 2019, doi: 10.1021/acsnano.9b04916.

[18] Y. Liu *et al.*, “α-MnO2 nanofibers/carbon nanotubes hierarchically assembled microspheres: Approaching practical applications of high-performance aqueous Zn-ion batteries,” *J. Power Sources*, vol. 443, no. October, p. 227244, 2019, doi: 10.1016/j.jpowsour.2019.227244.

[19] W. Sun *et al.*, “Zn/MnO2 Battery Chemistry with H+ and Zn2+ Coinsertion,” *J. Am. Chem. Soc.*, vol. 139, no. 29, pp. 9775–9778, 2017, doi: 10.1021/jacs.7b04471.

[20] N. Zhang *et al.*, “Rechargeable aqueous zinc-manganese dioxide batteries with high energy and power densities,” *Nat. Commun.*, vol. 8, no. 1, pp. 1–9, 2017, doi: 10.1038/s41467-017-00467-x.

[21] B. Wu *et al.*, “Graphene Scroll-Coated α-MnO2 Nanowires as High-Performance Cathode Materials for Aqueous Zn-Ion Battery,” *Small*, vol. 14, no. 13, pp. 1–8, 2018, doi: 10.1002/smll.201703850.

[22] T. Xiong *et al.*, “Defect Engineering of Oxygen-Deficient Manganese Oxide to Achieve High-Performing Aqueous Zinc Ion Battery,” *Adv. Energy Mater.*, vol. 9, no. 14, pp. 1–9, 2019, doi: 10.1002/aenm.201803815.

[23] W. Qiu *et al.*, “High-performance flexible quasi-solid-state Zn-MnO2 battery based on MnO2 nanorod arrays coated 3D porous nitrogen-doped carbon cloth,” *J. Mater. Chem. A*, vol. 5, no. 28, pp. 14838–14846, 2017, doi: 10.1039/c7ta03274a.

[24] S. Zhao *et al.*, “Unravelling the reaction chemistry and degradation mechanism in aqueous Zn/MnO2 rechargeable batteries,” *J. Mater. Chem. A*, vol. 6, no. 14, pp. 5733–5739, 2018, doi: 10.1039/c8ta01031e.

[25] Y. Fu *et al.*, “High-Performance Reversible Aqueous Zn-Ion Battery Based on Porous MnOx Nanorods Coated by MOF-Derived N-Doped Carbon,” *Adv. Energy Mater.*, vol. 8, no. 26, pp. 1–13, 2018, doi: 10.1002/aenm.201801445.

[26] M. Chamoun, W. R. Brant, C. W. Tai, G. Karlsson, and D. Noréus, “Rechargeability of aqueous sulfate Zn/MnO2 batteries enhanced by accessible Mn2+ ions,” *Energy Storage Mater.*, vol. 15, no. June, pp. 351–360, 2018, doi: 10.1016/j.ensm.2018.06.019.

[27] K. W. Nam, H. Kim, J. H. Choi, and J. W. Choi, “Crystal water for high performance layered manganese oxide cathodes in aqueous rechargeable zinc batteries,” *Energy Environ. Sci.*, vol. 12, no. 6, pp. 1999–2009, 2019, doi: 10.1039/c9ee00718k.

[28] T. Shoji and T. Yamamoto, “Charging and discharging behavior of zinc-manganese dioxide galvanic cells using zinc sulfate as electrolyte,” *J. Electroanal. Chem.*, vol. 362, no. 1–2, pp. 153–157, 1993, doi: 10.1016/0022-0728(93)80016-B.

[29] P. Oberholzer, E. Tervoort, A. Bouzid, A. Pasquarello, and D. Kundu, “Oxide versus Nonoxide Cathode Materials for Aqueous Zn Batteries: An Insight into the Charge Storage Mechanism and Consequences Thereof,” *ACS Appl. Mater. Interfaces*, vol. 11, no. 1, pp. 674–682, 2019, doi: 10.1021/acsami.8b16284.

[30] G. Fang *et al.*, “Suppressing Manganese Dissolution in Potassium Manganate with Rich Oxygen Defects Engaged High-Energy-Density and Durable Aqueous Zinc-Ion Battery,” *Adv. Funct. Mater.*, vol. 29, no. 15, pp. 1–9, 2019, doi: 10.1002/adfm.201808375.

[31] S. H. Kim and S. M. Oh, “Degradation mechanism of layered MnO2 cathodes in Zn/ZnSO4/MnO2 rechargeable cells,” *J. Power Sources*, vol. 72, no. 2, pp. 150–158, 1998, doi: 10.1016/S0378-7753(97)02703-1.

[32] M. Li *et al.*, “A Novel Dendrite-Free Mn2+/Zn2+ Hybrid Battery with 2.3 V Voltage Window and 11000-Cycle Lifespan,” *Adv. Energy Mater.*, vol. 9, no. 29, pp. 1–10, 2019, doi: 10.1002/aenm.201901469.

[33] R. Wang *et al.*, “Operando monitoring of ion activities in aqueous batteries with plasmonic fiber-optic sensors,” *Nat.*

Commun., vol. 13, no. 1, pp. 1–11, 2022, doi: 10.1038/s41467-022-28267-y.

[34] M. Liu *et al.*, “Tuning phase evolution of β-MnO2 during microwave hydrothermal synthesis for high-performance aqueous Zn ion battery,” *Nano Energy*, vol. 64, no. June, p. 103942, 2019, doi: 10.1016/j.nanoen.2019.103942.

[35] Y. Li *et al.*, “Reaction Mechanisms for Long-Life Rechargeable Zn/MnO 2 Batteries,” *Chem. Mater.*, vol. 31, no. 6, pp. 2036–2047, 2019, doi: 10.1021/acs.chemmater.8b05093.

[36] J. Huang *et al.*, “Polyaniline-intercalated manganese dioxide nanolayers as a high-performance cathode material for an aqueous zinc-ion battery,” *Nat. Commun.*, vol. 9, no. 1, pp. 1–8, 2018, doi: 10.1038/s41467-018-04949-4.

[37] M. Mateos, K. D. Harris, B. Limoges, and V. Balland, “Nanostructured Electrode Enabling Fast and Fully Reversible MnO2-to-Mn2+Conversion in Mild Buffered Aqueous Electrolytes,” *ACS Appl. Energy Mater.*, vol. 3, no. 8, pp. 7610–7618, 2020, doi: 10.1021/acsaem.0c01039.

[38] M. Mateos, N. Makivic, Y. S. Kim, B. Limoges, and V. Balland, “Accessing the Two-Electron Charge Storage Capacity of MnO2 in Mild Aqueous Electrolytes,” *Adv. Energy Mater.*, vol. 10, no. 23, 2020, doi: 10.1002/aenm.202000332.

[39] B. Lee *et al.*, “Critical Role of pH Evolution of Electrolyte in the Reaction Mechanism for Rechargeable Zinc Batteries,” *ChemSusChem*, vol. 9, no. 20, pp. 2948–2956, 2016, doi: 10.1002/cssc.201600702.

[40] J. Yang *et al.*, “Unravelling the Mechanism of Rechargeable Aqueous Zn–MnO2 Batteries: Implementation of Charging Process by Electrodeposition of MnO2,” *ChemSusChem*, vol. 13, no. 16, pp. 4103–4110, 2020, doi: 10.1002/cssc.202001216.

[41] O. Fitz *et al.*, “Electrolyte Study with in Operando pH Tracking Providing Insight into the Reaction Mechanism of Aqueous Acidic Zn//MnO2 Batteries,” *ChemElectroChem*, vol. 8, no. 18, pp. 3553–3566, 2021, doi: 10.1002/celc.202100888.

[42] I. Stoševski, A. Bonakdarpour, B. Fang, P. Lo, and D. P. Wilkinson, “Formation of MnxZny(OH)zSO4·5H2O – not intercalation of Zn – is the basis of the neutral MnO2/Zn battery first discharge reaction,” *Electrochim. Acta*, vol. 390, 2021, doi: 10.1016/j.electacta.2021.138852.

[43] S. J. Kim *et al.*, “Toward the Understanding of the Reaction Mechanism of Zn/MnO2Batteries Using Non-alkaline Aqueous Electrolytes,” *Chem. Mater.*, vol. 33, no. 18, pp. 7283–7289, 2021, doi: 10.1021/acs.chemmater.1c01542.

[44] H. Moon *et al.*, “Direct Proof of the Reversible Dissolution/Deposition of Mn2+/Mn4+ for Mild-Acid Zn-MnO2 Batteries with Porous Carbon Interlayers,” *Adv. Sci.*, vol. 8, no. 6, pp. 1–12, 2021, doi: 10.1002/advs.202003714.

[45] C. F. Bischoff *et al.*, “Revealing the Local pH Value Changes of Acidic Aqueous Zinc Ion Batteries with a Manganese Dioxide Electrode during Cycling,” *J. Electrochem. Soc.*, vol. 167, no. 2, p. 020545, 2020, doi: 10.1149/1945-7111/ab6c57.

[46] V. Mathew *et al.*, “Manganese and Vanadium Oxide Cathodes for Aqueous Rechargeable Zinc-Ion Batteries: A Focused View on Performance, Mechanism, and Developments,” *ACS Energy Lett.*, vol. 5, no. 7, pp. 2376–2400, 2020, doi: 10.1021/acsenergylett.0c00740.

[47] J. Lei, Y. Yao, Z. Wang, and Y. C. Lu, “Towards high-areal-capacity aqueous zinc-manganese batteries: Promoting MnO2dissolution by redox mediators,” *Energy Environ. Sci.*, vol. 14, no. 8, pp. 4418–4426, 2021, doi: 10.1039/d1ee01120k.

[48] K. J. Powell *et al.*, “Chemical speciation of environmentally significant metals with inorganic ligands. Part 5: The Zn2++ OH-, Cl -, CO3 2-, SO42-, and PO 43- systems (IUPAC Technical Report),” *Pure Appl. Chem.*, vol. 85, no. 12, pp. 2249–2311, 2013, doi: 10.1351/PAC-REP-09-03-05.

[49] K. A. Baltpurvins, R. C. Burns, G. A. Lawrance, and A. D. Stuart, “Use of the solubility domain approach for the modeling of the hydroxide precipitation of heavy metals from wastewater,” *Environ. Sci. Technol.*, vol. 30, no. 5, pp. 1493–1499, 1996, doi: 10.1021/es950421u.

[50] S. J. Hawkes, “All Positive Ions Give Acid Solutions in Water,” *J. Chem. Educ.*, vol. 73, no. 5, p. 516, 1996.

[51] T. Shoji, M. Hishinuma, and T. Yamamoto, “Zinc-manganese dioxide galvanic cell using zinc sulphate as electrolyte. Rechargeability of the cell,” *J. Appl. Electrochem.*, vol. 18, no. 4, pp. 521–526, 1988, doi: 10.1007/BF01022245.

[52] C. Qiu *et al.*, “The function of Mn2+ additive in aqueous electrolyte for Zn/δ-MnO2 battery,” *Electrochim. Acta*, vol. 351, p. 136445, 2020, doi: 10.1016/j.electacta.2020.136445.

[53] C. H. Kim, Z. Akase, L. Zhang, A. H. Heuer, A. E. Newman, and P. J. Hughes, “The structure and ordering of ε-MnO2,” *J. Solid State Chem.*, vol. 179, no. 3, pp. 753–774, 2006, doi: 10.1016/j.jssc.2005.11.042.

[54] H. Chen *et al.*, “Reunderstanding the Reaction Mechanism of Aqueous Zn–Mn Batteries with Sulfate Electrolytes: Role of the Zinc Sulfate Hydroxide,” *Adv. Mater.*, vol. 34, p. 2109092, 2022, doi: 10.1002/adma.202109092.

[55] C. M. Julien, M. Massot, and C. Poinsignon, “Lattice vibrations of manganese oxides: Part I. Periodic structures,” *Spectrochim. Acta - Part A Mol. Biomol. Spectrosc.*, vol. 60, no. 3, pp. 689–700, 2004, doi: 10.1016/S1386-1425(03)00279-8.

[56] D. Perez-Antolin, I. Sáez-Bernal, A. Colina, and E. Ventosa, “Float-charging protocol in rechargeable Zn–MnO2 batteries: Unraveling the key role of Mn2+ additives in preventing spontaneous pH changes,” *Electrochem. commun.*, vol. 138, no. April, p. 107271, 2022, doi: 10.1016/j.elecom.2022.107271.

[57] T. Labbaye *et al.*, “In situ Raman spectroscopy for growth monitoring of vertically aligned multiwall carbon nanotubes in plasma reactor,” *Appl. Phys. Lett.*, vol. 105, no. 21, 2014, doi: 10.1063/1.4902915.

[58] C. Julien and M. Massot, “Spectroscopic studies of the local structure in positive electrodes for lithium batteries,” *Phys. Chem. Chem. Phys.*, vol. 4, no. 17, pp. 4226–4235, 2002, doi: 10.1039/b203361e.

[59] J. E. Post, D. A. McKeown, and P. J. Heaney, “Raman spectroscopy study of manganese oxides: Layer structures,” *Am. Mineral.*, vol. 106, no. 3, pp. 351–366, 2021, doi: 10.2138/am-2021-7666.

[60] A. Moezzi, M. B. Cortie, and A. M. McDonagh, “Zinc hydroxide sulphate and its transformation to crystalline zinc oxide,” *Dalt. Trans.*, vol. 42, no. 40, pp. 14432–14437, 2013, doi: 10.1039/c3dt51638e.

[61] L. Liu *et al.*, “Alkali Ions Pre-Intercalated Layered MnO2 Nanosheet for Zinc-Ions Storage,” *Adv. Energy Mater.*, vol. 11, no. 31, 2021, doi: 10.1002/aenm.202101287.

[62] A. Singh, O. Sel, H. Perrot, V. Balland, B. Limoges, and C. Laberty-Robert, “Towards a high MnO2loading and gravimetric capacity from proton-coupled Mn4+/Mn2+reactions using a 3D free-standing conducting scaffold,” *J. Mater. Chem. A*, vol. 9, no. 3, pp. 1500–1506, 2021, doi: 10.1039/d0ta10685b.

[63] A. O. Efremova, A. I. Volkov, E. G. Tolstopyatova, and V. V. Kondratiev, “EQCM study of intercalation processes into electrodeposited MnO2 electrode in aqueous zinc-ion battery electrolyte,” *J. Alloys Compd.*, vol. 892, p. 162142, 2022, doi: 10.1016/j.jallcom.2021.162142.

[64] J. Livage, M. Henry, and C. Sanchez, “Sol-gel chemistry of transition metal oxides,” *Prog. Solid State Chem.*, vol. 18, no. 4, pp. 259–341, 1988, doi: 10.1016/0079-6786(88)90005-2.

[65] I. Zadok *et al.*, “Unexpected hydroxide ion structure and properties at low hydration,” *J. Mol. Liq.*, vol. 313, p. 113485, 2020, doi: 10.1016/j.molliq.2020.113485.

[66] N. Agmon, “Mechanism of hydroxide mobility,” *Chem. Phys. Lett.*, vol. 319, no. 3–4, pp. 247–252, 2000, doi: 10.1016/S0009-2614(00)00136-6.

[67] A. Cuenca, J. Agrisuelas, R. Catalán, J. J. García-Jareño, and F. Vicente, “Motional Resistance Evaluation of the Quartz Crystal Microbalance to Study the Formation of a Passive Layer in the Interfacial Region of a Copper|Diluted Sulfuric Solution,” *Langmuir*, vol. 31, no. 35, pp. 9655–9664, 2015, doi: 10.1021/acs.langmuir.5b02233.

[68] N. Shpigel, M. D. Levi, and D. Aurbach, “EQCM-D technique for complex mechanical characterization of energy storage electrodes: Background and practical guide,” *Energy Storage Mater.*, vol. 21, no. April, pp. 399–413, 2019, doi: 10.1016/j.ensm.2019.05.026.

[69] P. Lemaire, T. Dargon, D. Alves Dalla Corte, O. Sel, H. Perrot, and J. M. Tarascon, “Making Advanced Electrogravimetry as an Affordable Analytical Tool for Battery Interface Characterization,” *Anal. Chem.*, vol. 92, no. 20, pp. 13803–13812, 2020, doi: 10.1021/acs.analchem.0c02233.

[70] M. Wild *et al.*, “Lithium sulfur batteries, a mechanistic review,” *Energy Environ. Sci.*, vol. 8, no. 12, pp. 3477–3494, 2015, doi: 10.1039/c5ee01388g.

[71] C. David *et al.*, “Thermodynamics and kinetics of the dissolution of ZnO nanoparticles followed by AGNES,” *J. Phys. Chem. C*, vol. 116, pp. 11758–11767, 2012.

[72] E. V. Shkol’Nikov, “Thermodynamic characterization of the amphoterism of hydroxides and oxides of scandium subgroup elements in aqueous media,” *Russ. J. Appl. Chem.*, vol. 82, no. 12, pp. 2098–2104, 2009, doi: 10.1134/S1070427209120040.

[73] K. A. Baltpurvins, R. C. Burns, G. A. Lawrance, and A. D. Stuart, “Effect of electrolyte composition on zinc hydroxide precipitation by lime,” *Water Res.*, vol. 31, no. 5, pp. 973–980, 1997, doi: 10.1016/S0043-1354(96)00327-2.

[74] Z. Ye, T. Li, G. Ma, Y. Dong, and X. Zhou, “Metal-Ion (Fe, V, Co, and Ni)-Doped MnO2 Ultrathin Nanosheets Supported on Carbon Fiber Paper for the Oxygen Evolution Reaction,” *Adv. Funct. Mater.*, vol. 27, no. 44, 2017, doi: 10.1002/adfm.201704083.